https://doi.org/10.1016/j.conbuildmat.2023.130658

Stress-strain models for ultra-high performance concrete (UHPC) and ultra-high performance fiber-reinforced concrete (UHPFRC) under triaxial compression

S.S. Zhang [1*], J.J. Wang [2], Guan Lin [3*], T. Yu [4], D. Fernando [5]

[1] Professor, School of Civil and Hydraulic Engineering, Huazhong University of Science and Technology, Wuhan, China.
[2] PhD Candidate, School of Civil and Hydraulic Engineering, Huazhong University of Science and Technology, Wuhan, China.
[3] Assistant Professor, Department of Ocean Science and Engineering, Southern University of Science and Technology, Shenzhen, Guangdong 518055, China.
[4] Professor, Department of Civil and Environmental Engineering, The Hong Kong Polytechnic University, Hung Hom, Kowloon, Hong Kong, China.
[5] Professor, School of Engineering, University of Edinburgh, Scotland, EH9 3FG, United Kingdom.

Abstract: The constitutive behavior of Ultra-high performance concrete (UHPC) and ultra-high performance fiber reinforced concrete (UHPFRC) under multiaxial stresses, which has not been well understood, needs to be urgently investigated in order to meet an increasing demand for use of UHPC/UHPFRC in construction. This paper therefore presents an experimental study on the triaxial compressive behavior of UHPC and UHPFRC under triaxial compression. The compressive strength of UHPC and UHPFRC in present study are up to 126.9 and 151.5 MPa, respectively. The test variables included the level of lateral hydraulic pressure, steel fiber volume fraction, and uniaxial compressive strength of UHPC and UHPFRC. The present experimental study provides the much-needed systematic test data on the triaxial compressive behavior of UHPC/UHPFRC. The test results showed that the lateral hydraulic pressure significantly enhanced both the strength and ductility of UHPC and UHPFRC. The presence of steel fibers had significant effects on the axial stress-axial strain behavior and the dilation behavior of UHPC and UHPFRC. Finally, new axial stress-axial strain models as well as a new equation for the axial strain-lateral strain relationship for UHPC and UHPFRC were first proposed.

Keywords: UHPC; UHPFRC; triaxial compression; stress-strain model; active confinement; FRP confined concrete; concrete filled steel tube

*Corresponding author: S.S. Zhang, shishun@hust.edu.cn; G. Lin, ling@sustech.edu.cn.

1. Introduction

Ultra-high performance concrete (UHPC) and ultra-high performance fiber reinforced concrete (UHPFRC) have become a promising alternative to conventional materials in the construction of new structures due to its superior mechanical properties and durability. UHPC and UHPFRC are characterized with a high cement and silica fume content and a low water-to-cement ratio, leading to an ultra-high compressive strength and a low permeability [1–4]. The raw materials for making UHPC and UHPFRC typically include water, cement, silica fume, high-range superplasticizer, supplemental fine materials (e.g., fly ash, quartz powder, silica powder), quartz sand, and fibers [1,5–10]. With the consistent growth of application of UHPC/UHPFRC in new construction, a large number of studies have been conducted on its mix proportions, production and/or curing procedures, as well as mechanical behavior of structural members made of UHPC/UHPFRC [3,4,6,7,11–21]. However, very limited studies have investigated the behavior of UHPC/UHPFRC under multiaxial stresses. The behavior of concrete under multiaxial stresses has long been recognized as an important element in understanding the behavior of concrete structural members in practice which are generally subjected to various loading conditions. The constitutive behavior of concrete under multiaxial stresses are key information necessary for finite element modelling of concrete structural members. One of the most typical multiaxial stress states is the triaxial compressive stress state with two equal lateral compressive stresses (commonly applied through a hydraulic pressure) in combination with axial compression, which is essential for the modelling of steel spiral and stirrup confined concrete [22], concrete filled in steel tube [23] and fiber reinforced polymer (FRP)-confined concrete members [19,24–28]. The tests on concrete under combined axial compression and hydraulic pressure are referred to as hydraulic pressure tests hereafter. Particularly, concrete with a constant lateral pressure throughout the loading process is commonly referred to as concrete with active confinement [29,30].

According to the literature, in terms of compressive strength, concrete with a strength ranging from 20 to 50 MPa is referred to as normal-strength concrete (NSC), while high-strength concrete (HSC), high-performance concrete (HPC), or high-performance fiber reinforced concrete (HPFRC) generally has a compressive strength exceeding 50 MPa [31,32]. Ultra-high strength concrete (UHSC) and UHPC/UHPFRC are generally characterized with a compressive strength of at least 120 MPa [33,34]. UHPC/UHPFRC generally does not contain coarse aggregates, while HSC/UHSC/FRC contains coarse aggregates.

A large number of studies have been carried out on the triaxial compressive behavior of NSC, HSC, and fiber reinforced concrete (FRC) [29,30,35–46]. Following the pioneer study of Richart et al. [35], extensive experimental studies have been conducted on NSC under active confinement [36–39], leading to accurate stress-strain models [38,39]. The behavior of HSC under triaxial stress states has also been extensively investigated and a number of failure criteria and stress-strain models for HSC have been proposed [29,37–43]. The effect of steel fibers on the triaxial compressive behavior of HSC was found not significant [44,45].

Compared with NSC and HSC, limited studies have been conducted on the triaxial compressive behavior of UHSC and UHPC [47–52]. Wang et al. [47] investigated the triaxial compressive behavior of cylindrical UHSC specimens with coarse aggregate (48 mm in diameter and 96 mm in height, i.e., 48 mm × 96 mm) with a compressive strength over 200 MPa through hydraulic pressure tests. The tests were performed over an extensive range of confining pressures with large gaps (0, 25, 50, 100, 200 and 400 MPa). Very limited studies have been conducted so far on the triaxial compressive behavior of UHPC/UHPFRC through hydraulic pressure tests [45–49]. Wu et al. [49] investigated the effect of steel fiber content (0-2.4%) on the triaxial compressive behavior of UHPC (called reactive powder concrete, RPC, in the original paper) with a compressive strength higher than 140 MPa through tests on 43.6 mm × 130 mm cylinder specimens. It was found that the failure mode of UHPC specimens was affected by the steel fiber content, but the peak axial stress was little affected. Vogel et al. [50] tested four 150 mm × 300 mm cylindrical and five 100-mm-length cubic UHPC specimens. The compressive strength of their UHPC was measured to be 123 MPa and 149 MPa respectively. They found that the triaxial compressive strength of UHPC follows a power law function of the confining pressure and the development of triaxial compressive strength of UHPC was different from those of NSC and HSC. Strain data and stress-strain curves of the tested specimens were not reported in their study. Wang et al. [51] conducted hydraulic pressure tests on both UHPC and UHPFRC cylindrical specimens (50 mm × 100 mm) with the confining pressure ranging from 0 to 50 MPa. The compressive strength of their UHPC/UHPFRC ranged from 119.8 MPa to 148.5 MPa. For most of their specimens, the axial stress decreased quickly after the peak stress even though the confining pressure was high, which is different with the results from [30,45,46,52]. They found that the enhancement in compressive strength of UHPFRC at a given hydraulic pressure was slightly lower than that of UHPC. Wu et al [52] performed a series tests of UHPC and UHPFRC with 0.5%, 1.0% and 1.5% steel fiber addition cylindrical specimens (50 mm × 100 mm), however, the uniaxial compressive strength of their UHPC and UHPFRC were 75.57 MPa, 84.07 MPa, 93.26 MPa and 99.98 MPa much lower than the general understanding [20,21].

The triaxial compressive behavior of UHPC or UHPFRC has not been fully understood based on the limited studies reviewed above. No reliable model has been proposed to accurately capture the axial stress-axial strain curves of UHPC or UHPFRC under triaxial compression. This paper therefore presents the results of an experimental program on UHPC and UHPFRC subjected to triaxial compression through hydraulic pressure tests. Various hydraulic pressures from 0 to 50 MPa were applied on cylindrical UHPC and UHPFRC specimens. In addition, two steel fiber volume ratios and two uniaxial compressive strengths were included as the test variables. The experimental program provided a much-needed supplement to the very limited existing test data on the triaxial compressive behavior of UHPC and UHPFRC. The test results showed that the confining pressure significantly enhanced both the strength and ductility of UHPC and UHPFRC. The presence of steel fibers had significant effects on the axial stress-axial strain behavior and the dilation behavior of UHPC. It was also found that existing models developed for NSC failed to predict the axial stress-axial strain behavior of UHPC and UHPFRC subjected to triaxial compression; new axial stress-axial strain models were therefore proposed in the present study. In addition, a new equation was proposed for the prediction of the axial strain-lateral strain relationship of the test UHPC and UHPFRC specimens.

2. Experimental program

2.1. Test specimens

In total, 14 UHPC and 18 UHPFRC cylindrical specimens (with a diameter of 50 mm and a height of 100 mm) were prepared and tested under triaxial compression with the confining pressure ranging from 0 to 50 MPa. Such a range of confining pressures generally covers the typical stress states of concrete in practical engineering (e.g., steel confined concrete, FRP-confined concrete) [16,19–25]. Two nominally identical specimens were tested for each specimen configuration except for the specimens with a confining pressure of 0 MPa (i.e., specimens under uniaxial compression). Two concrete grades were covered for UHPC and the corresponding UHPFRC. The details of the test specimens are summarized in Table 1. Each specimen was given a name which starts with "UHPC" or "UHPFRC" representing the concrete type, followed by "1" or "2" denoting the higher or lower concrete strength grade, and then a two digit number representing the magnitude of the confining pressure. The name ends with one digit number (if exists) to differentiate between the two nominally identical specimens. For example, specimen UHPC-1-50-1 refers to the first specimen of the two nominally identical UHPC specimens with higher uniaxial concrete strength tested under a confining pressure of 50 MPa.

2.2. Materials and specimen preparation

In the present study, UHPC was produced using the following raw materials: Portland cement, silica fume, fly ash, quartz sand, quartz powder, superplasticizer and water. The composition of UHPFRC is the same as UHPC, expect that straight steel fibers of 2% in volume fraction were added in the former. The key properties of the steel fibers are shown in Table 2. The mix proportions of UHPC and UHPFRC are given in Table 3. To achieve two concrete grades of UHPC and UHPFRC, two different values of water-to-binder ratio and slightly different amounts of superplasticizer were adopted as listed in Table 3.

The mixing, casting and curing process of UHPC and UHPFRC specimens included the following steps: (1) dry-mixing cement, silica fume, fly ash, quartz sand, quartz powder in a concrete mixer for around 3 minutes; (2) adding water and superplasticizer into the mixture and continuing mixing for around 7 minutes; (3) for UHPFRC, adding dispersed steel fibers into the mixture and mixing for around 5 minutes; (4) pouring the mixture into a plastic mold and vibrating the mold to ensure the compactness of concrete; (5) curing the specimens in room temperature for 24 hours before demolding, followed by steam-curing with a temperature of 90 ±3℃ for 48 hours in accordance with ASTM C1856/C1856M-17 [33]; and (6) curing the specimens in a curing room with a temperature of 20±2℃ for at least 28 days. After curing, uniaxial compression tests were carried out on three identical *cylindrical specimens* (with a diameter of 100 mm and a height of 200 mm) for each group of UHPC and UHPFRC and the results are presented in Table 4. Before the triaxial compression tests, some voids on the surface of each specimen were filled with high-strength gypsum to ensure a smooth surface for well receiving the lateral pressure. Both ends of each specimen were capped with high-strength gypsum to ensure that the ends were perpendicular to the specimen axis and the axial load was uniformly applied on the cross-section (Fig. 1).

2.3. Test set-up and instrumentation

Both uniaxial and triaxial compression tests were performed on an MTS Model 815 Rock Mechanics Test System as shown in Fig. 2. While this system was designed for testing rock specimens, it is also suitable for testing UHPC and UHPFRC specimens due to their ultra-high compressive strength comparable to that of rock. The machine mainly consists of a vertical servo-controlled electro-hydraulic actuator with a load capacity of 4600 kN and a high-pressure vessel of up to 140 MPa (Fig. 2). During the loading process, the vessel is filled with hydraulic oil to apply the lateral confining pressure on the surface of the test specimen. To avoid the penetration of hydraulic oil into the specimens and thus ensure an effective application of lateral confining pressure, a heat-shrinkable tube made of fluorinated ethylene propylene was used to wrapping each test specimen (except for the specimens with a zero hydraulic pressure) before testing.

For each test specimen, two axial strain extensometers at 180° apart covering a mid-height region of 50 mm were installed to measure the axial strains of the specimen. The axial strains of the specimen could also be obtained from the full-height axial shortenings recorded by the MTS testing system. In addition, a ring chain type extensometer was installed around the mid-height section of each specimen for measuring the lateral strains. The layouts of the extensometers are shown in Fig.3. The axial loads, confining pressures, axial strains, and lateral strains were recorded by a data acquisition system for every 0.2 seconds.

2.4. Test procedure

In the present paper, compressive stresses and strains are defined to be positive. The loading path of the specimens subjected to a hydraulic pressure is shown in Fig. 4: the axial stress σ_1 and the hydraulic pressure ($\sigma_2 = \sigma_3$) were first applied to the specimen simultaneously with a load control rate of 0.1 MPa/s until the targeted value of the confining pressure (f_l) was reached (Stage 1); after that, the confining pressure ($\sigma_2 = \sigma_3$) was kept constant and the axial load was applied onto the specimen with a displacement control rate of 0.001 mm/s (Stage 2). During Stage 2, the axial stress σ_1 increased to the compressive strength of the specimen (f_{cc}) and finally dropped as a result of failure. The maximum confinement ratio (f_l/f'_{co}, where f'_{co} is the uniaxial UHPC/UHPFRC strength) was approximately 0.5.

3. Experimental observations and results

3.1. Failure modes

3.1.1. Specimens under uniaxial compression

Both the UHPC and UHPFRC specimens failed with an explosive sound when the peak stress was reached. Typical failure modes of the UHPC and UHPFRC specimens are shown in Fig. 5. It can be seen that the UHPC and UHPFRC specimens exhibited significantly different failure modes. The UHPC specimens were crushed and split into several longitudinal pieces shortly after the peak stress was reached, while the UHPFRC specimens had more smeared cracks with a more gradual failure process after the peak stress accompanied with snapping pulling-out sounds of steel fibers. Compared with the UHPC specimens with a sudden brittle failure, the UHPFRC specimens exhibited a certain level of ductility with a progressive failure due to the existence of steel fibers. The above observations on the failure modes of UHPC and UHPFRC specimens under uniaxial compression are consistent with those reported by other researchers [11,23,47,51,52].

3.1.2. Specimens under triaxial compression

Fig. 6 shows failure modes of all UHPC and UHPFRC specimens under triaxial compression. A sharp diagonal major crack can be observed in the specimens, which is significantly different from the specimens under uniaxial compression (see Fig. 5). In addition to the major diagonal crack, some minor multiple diagonal cracks could also be observed on the surface of the specimen. It could be seen that an increase in confining pressure leads to a smaller inclined angle (with respect to horizon) of the major diagonal crack and a smaller diagonal crack width as shown in Fig. 6. The uniaxial concrete compressive strength does not seem to have an obvious effect on the failure modes of UHPC and UHPFRC specimens under various confining pressures (by comparing UHPC/UHPFRC-1 and UHPC/UHPFRC-2 specimens).

3.2. Uniaxial compressive strength and corresponding strain

The test results of the specimens under uniaxial compression, including the average compressive strength and the corresponding axial strain are shown in Table 4. The average uniaxial compressive strengths of UHPC-1 and UHPC-2 were measured to be 126.9 MPa and 101.0 MPa, respectively, while those of UHPFRC-1 and UHPFRC-2 were 151.5 MPa and 127.1 MPa, respectively. The axial strains at peak stress of UHPFRC specimens are larger than those of UHPC specimens. The elastic moduli, calculated by the slope of the stress-strain curve between the axial strain of 0.00005 and that at 40% of the ultimate stress (according to ASTM C469/C469M [53]), of the test specimens are also listed in the table.

3.3. Axial stress-strain curves

The axial stress-strain (axial strain and lateral strain) curves of the test UHPC and UHPFRC specimens under various confining pressures are shown in Fig. 7 and Fig. 8, respectively. The key test results, including the compressive strength (i.e., peak stress f_{cc}) and the corresponding axial strain (ε_{cc}), are listed in Table 5. The axial stresses were obtained from the applied axial loads divided by the concrete cross-sectional area. The axial strain extensometers covering a mid-height of 50 mm were used to obtain the axial strains; the lateral strains were obtained from the readings of the hoop ring chain type extensometer (Fig. 3). It should be noted that two UHPC specimens (UHPC-1-50-1 and UHPC-2-50-1) under a confining pressure of 50 MPa experienced premature failure due to the damage of the heat-shrinkable tube, thus their results are excluded in the subsequent discussions. Fig. 7 and Fig. 8 show that the stress-strain curves of two nominally identical specimens are generally close to each other, with the maximum difference in peak stress being 11.4% for specimen UHPFRC-2-50.

Fig. 9 shows the normalized axial stress (σ_c/f'_{co}) and normalized axial strain ($\varepsilon_c/\varepsilon_{co}$) of specimens UHPC-1 and UHPFRC-2 which had similar uniaxial compressive strengths. The axial stress-strain curves of UHPC and UHPFRC specimens under triaxial compression generally consist of three branches: an ascending first branch up to the peak stress point (ε_{cc}, f_{cc}); a descending branch after the peak stress; and a third branch which is much flatter (i.e., the stresses reduced much more gradually) than the second branch or even with a residual stress plateau. Compared with UHPC specimens, the first branch of the stress-strain curves of UHPFRC specimens seems to be longer and more curved especially for the specimens with a relatively high hydraulic pressure (40 MPa and 50 MPa). The UHPFRC specimens generally possess a more gradual stress reduction for the second branch (i.e., flatter second branch) compared with the UHPC specimens under the same hydraulic pressure as shown in Fig. 9, indicating the beneficial effects of steel fibers on the ductility of concrete. It is also seen from Fig. 9 that the addition of steel fibers enhances the residual stress; however, the enhancement in peak axial stress due to a confining pressure is reduced compared with that of UHPC without steel fibers.

In addition, it can be seen that the steep descending second branch of UHPC specimens is a little affected by the hydraulic pressure; however, the increase in hydraulic pressure evidently reduces the slope of the descending second branch of UHPFRC specimens (i.e., a slower reduction in the axial stress with respect to the axial strain). Fig. 8 also shows that the concrete grade has little effects on the shape of the stress-strain curves of UHPFRC specimens; however, specimens with a lower compressive strength (i.e., UHPFRC-2 series) obviously have a larger axial strain at the peak stress, leading to a longer portion before the peak stress, than the corresponding specimens with a higher compressive strength (i.e., UHPFRC-1 series). However, the effect of concrete grade on the stress-strain behavior of UHPC specimens was not obvious (Fig. 7). The axial stresses of UHPC specimens with a zero hydraulic pressure dropped to nearly zero rapidly after the peak stress while the axial stresses of UHPFRC specimens dropped more gradually to a residual stress.

3.4. Axial strain-lateral strain curves

The axial strain-lateral strain curves of specimens under various confining pressures are shown in Fig. 10 and Fig. 11 for UHPC and UHPFRC specimens, respectively. Similar to NSC, the axial strain-lateral strain curves of UHPC/UHPFRC specimens with hydraulic pressure generally consist of two linear portions connected smoothly at the transition region. The curves of UHPC or UHPFRC specimens with different confining pressures are close to each other during the initial loading stages, but they diverge obviously in the second portion. The normalized axial strain ($\varepsilon_c/\varepsilon_{co}$) and lateral strain ($\varepsilon_l/\varepsilon_{co}$) curves of specimens UHPC-1 and UHPFRC-2 are shown in Fig. 12. For the UHPC specimens with a zero pressure, the lateral strains after the peak stress increased rapidly due to the brittle failure of the specimen, leading to an almost vertical line for the second portion of the axial strain-lateral strain curve. However, the UHPFRC specimens without confining pressure failed in a much more gradual process, leading to an inclined second portion after the sudden transition point as shown in Fig. 12. At a given axial strain, the lateral strain of an UHPC or UHPFRC specimen with a higher hydraulic pressure is smaller in magnitude, indicating that the dilation of concrete is more effectively restricted by a larger confining pressure. Fig. 12 shows that the dilations of UHPC specimens are generally larger than UHPFRC specimens, especially for those with confining pressures of 0, 10 and 30 MPa.

4. Proposed axial stress-axial strain models

Extensive research has been conducted on NSC under active confinement, leading to numerous axial stress-axial strain models (simply referred to as stress-strain models hereafter) [38,39,54,55]. However, it was found that these models are not able to well predict the stress-strain behavior of UHPC/UHPFRC due to its different shape characteristics of stress-strain curve compared with NSC or HSC as mentioned earlier. The stress- strain curve of unconfined UHPC/UHPFRC exhibits a much steeper descending branch after the peak stress due to its ultra high strength as demonstrated by existing studies and as shown in Fig. 7 and Fig. 8. As a result, it is necessary to develop new stress-strain models which are suitable for both unconfined and actively confined UHPC and UHPFRC. In this section, the stress-strain model proposed by Popovics [55] with some adaptions (Model I) is first evaluated, followed by a new stress-strain model (Model II). Model I employs a single equation for describing the entire stress-strain curve, which is largely controlled by the peak axial stress and the corresponding strain, while Model II is a two-segment stress-strain model which adopts separate equations for the ascending and descending branches. A test database was assembled for the regression analysis for obtaining the key parameters of the two models. The test data used in the regression analysis included the UHPC (including RPC) and UHPFRC specimens of the present study as well as those from existing studies [48–51]. Only the specimens with a uniaxial compressive strength higher than 120 MPa and without coarse aggregates were included in the test database. The test database included totally 25 RPC specimens and 39 UHPC or UHPFRC specimens as listed in Table 6.

4.1. Proposed axial stress-axial strain models

4.1.1. Model I

The equation of Popovics [55] has been widely employed in depicting the axial stress-axial strain curves of unconfined or actively confined NSC and HSC [29,39,54–59]. Therefore, Popovics' equation is adopted in Model I, which is described in the following equation:

$$\frac{\sigma_c}{f_{cc}} = \frac{(\varepsilon_c/\varepsilon_{cc}) \times r}{r - 1 + (\varepsilon_c/\varepsilon_{cc})^r} \quad (1)$$

$$r = \frac{E_c}{E_c - f_{cc}/\varepsilon_{cc}} \quad (2)$$

where σ_c and ε_c are the axial stress and the axial strain; f_{cc} and ε_{cc} are respectively the peak axial stress and the corresponding axial strain; E_c is the elastic modulus of UHPC/UHPFRC, which can be calculated in $E_c = 35497.50 + 78.00 \times f'_{co}$ (f'_{co} is the compressive strength of unconfined UHPC/UHPFRC) proposed by Teng et al [7] This equation was found to be reasonably accurate in predicting the test UHPC/UHPFRC specimens in the present study.

4.1.2. Model II

It was later found that Model I does not perform very well in capturing the descending branch of UHPC/UHPFRC. Therefore, Model II, which is a two-segment stress-strain model with separate equations for the ascending and descending branches, is proposed. The Popovics' [55] equation (Eq. 1) is still employed for the ascending branch, while the following fractional equation is employed for the descending branch:

$$\sigma_c = f_{cres} + \frac{f_{cc} - f_{cres}}{1 + n \times \left(\frac{\varepsilon_c}{\varepsilon_{cc}} - 1\right)^2} \quad \text{for } \varepsilon_c > \varepsilon_{cc} \quad (3)$$

where $n = \frac{2}{1+100V_{sf}}$ (where V_{sf} is the steel fiber volume ratio) is the curve-fitting factor for the post-peak descending branch to distinguish the influence of steel fiber on the stress-strain relationship; f_{cres} is the residual axial stress as discussed in detail in Section 4.3. Eq. (3) has the following characteristics: (I) when $\varepsilon_c = \varepsilon_{cc}$, $\sigma_c = f_{cc}$; (II) when $\varepsilon_c = +\infty$, $\sigma_c = f_{cres}$.

It is evident that the determination of peak stress point $(f_{cc}, \varepsilon_{cc})$ is critical in both Model I and Model II, and the residual axial stress f_{cres} is needed in Model II to generate the entire stress- strain curve. The calculations of these parameters are discussed in detail in the following sections.

4.2. Peak axial stress f_{cc} and corresponding strain ε_{cc}

Similar to NSC and HSC under triaxial compression, the peak axial stress f_{cc} of UHPC or UHPFRC increases with the confining pressure f_l. The relationships between the peak axial stress and the confining pressure for all the collected specimens are shown in Fig. 13. It can be seen that the addition of steel fibers slightly reduces the axial stress enhancement for the specimen in the present study and Wang et al.'s study [51], but the effect of steel fibers is not significant in Wu et al.'s study [49]. A regression analysis of the test results led to the following equation for the peak axial stress f_{cc}:

$$\frac{f_{cc}}{f'_{co}} = 1 + (3.1 - 16V_{sf}) \times \left(\frac{f_l}{f'_{co}}\right)^{0.7} \tag{4}$$

Similarly, the following equation was obtained for the axial strain at peak axial stress ε_{cc} based on a regression analysis of the test results:

$$\frac{\varepsilon_{cc}}{\varepsilon_{c0}} = 1 + (12 + 100V_{sf}) \times \left(\frac{f_l}{f'_{co}}\right)^{1.05} \tag{5}$$

The performance of Eq. (4) and Eq. (5) are shown in Figs. 13 and 14, respectively. It can be seen that the two equations fit the test results very well. The coefficient of determination (R^2) of Eq. (4) for UHPC and UHPFRC specimens are 0.85 and 0.88, respectively. The coefficient of determination (R^2) in predicting the axial strain at peak axial stress ε_{cc} for UHPC and UHPFRC specimens are 0.93 and 0.92, respectively.

4.3. Residual axial stress f_{cres}

As discussed in the preceding sections, a residual axial stress (f_{cres}) may exist after the descending branch of the stress-strain curve of concrete under triaxial compression [39,41,58,60–63]. As shown in Figs. 7 and 8, this residual axial stress of UHPC and UHPFRC generally increases as the hydraulic pressure increases. The definition of such residual axial stress in concrete, however, varies in different studies [41,62,63]. Xie et al. [41] considered the residual axial stress at the point where the slope of the remaining part of the descending curve is less than 2% of the initial slope of the ascending branch. Smith [62] defined the axial stress carried by concrete at a lateral strain of 0.03 as the residual axial stress. This method, however, is not applicable to some specimens with a long post-peak descending branch (e.g., specimens UHPFRC-1-10 and UHPFRC-2-10) as shown in Fig. 8. Samani and Attard [63] took the end points of axial stress-axial strain curves as the residual stress and found these definitions are close to the reported residual stress values in most cases. In the present study, the residual axial stress is defined based on the methods of Xie et al. [41] and Smith [62]. In the present study, a residual stress plateau is assumed to appear when the slope magnitude of the descending curve is less than 2% of the elastic modulus of UHPC/UHPFRC and the axial stress at the end of the axial stress-strain curve is then defined as the residual axial stress f_{cres}. If no stress plateau was identified for a test specimen, this specimen was excluded in the subsequent analysis and discussion for the residual axial stress.

The relationships between the normalized residual axial stress f_{cres}/f'_{co} and the confinement ratio f_l/f'_{co} for the test UHPC and UHPFRC specimens which had a stress plateau are shown in Fig. 15. Fig. 15 shows that the normalized residual stress is an almost linear function of the confinement ratio. A regression of the test results led to the following linear equation for f_{cres}:

$$\frac{f_{cres}}{f'_{co}} = 9V_{sf} + 4.7 \times \left(\frac{f_l}{f'_{co}}\right) \tag{6}$$

As shown in Fig. 15, Eq. (6) provides accurate estimations for the residual axial stresses of the test specimens of the present study (V_{sf} = 2%). It should be noted that, due to the limit test data on UHPFRC with various values of V_{sf}, only the UHPFRC specimens of the present study with V_{sf} = 2% were used for the regression analysis of Eq. (6). Eq. (6) may need refinement in the future when more test data on UHPFRC become available.

4.4. Comparison with test results

The comparison between the predictions of Model I and Model II and test results for the test specimens in the present study and Wang et al. [48] are shown in Fig. 16. The predicted curve of each specimen under triaxial compression terminated when the average experimental ultimate axial strain was reached. It can be seen from Figs. 16(a) and (b) that the predictions of Model II agree reasonably well with the test curves of UHPC specimens with various confining pressures, while Model I fails to capture the sudden load drop after the peak stress and the residual axial stress especially for those with a relatively high confining pressure. Figs. 16(c) and (d) show that both Model I and Model II slightly overestimate the peak axial stress of UHPFRC specimens. The performance of Model I and Model II is very close for the UHPFRC specimens in the present study. Figs. 16 (c) and (d) show the comparison of the test results from Wang et al. [48] and the predictions from Model I and Model II. It can be seen that Model II captures the test curves more accurately. In general, Model II performs well in predicting the axial stress-axial strain curves of the UHPC and UHPFRC specimens under triaxial compression.

5. Proposed equations for axial strain-lateral strain relationship

The axial strain-lateral strain relationship is an essential element for understanding the dilation behavior of UHPC and UHPFRC under various confining pressures. Many equations have been proposed for the axial strain-lateral strain relationship of NSC or HSC. A typical and widely adopted one is the equation of Teng et al [64] originally proposed for unconfined, actively confined, and fiber reinforced polymer (FRP)-confined concrete, which is described in the following equation:

$$\frac{\varepsilon_c}{\varepsilon_{co}} = 0.85\left(1 + 8\frac{\sigma_l}{f'_{co}}\right) \times \left\{\left[1 + 0.75\left(-\frac{\varepsilon_l}{\varepsilon_{co}}\right)\right]^{0.7} - \exp\left[-7\left(-\frac{\varepsilon_l}{\varepsilon_{co}}\right)\right]\right\} \quad (7)$$

where σ_l is the confining pressure (= f_l for active confinement); and ε_l is the lateral strain.

Fig. 17 shows the comparison of the predictions with Eq. (7) and the test curves of the UHPC and UHPFRC specimens in the present study (the test curves of the specimens in the existing studies are not reported). The predicted curve of each specimen terminated when the average experimental ultimate lateral strain was reached. It can be seen from Fig. 17 that the predictions of Eq. (7) generally overestimate the test curves of UHPC and UHPFRC specimens except for the specimens with 10 MPa hydraulic pressure. This comparison indicates that the confinement effectiveness of UHPC/UHPFRC is lower than that of NSC.

Teng et al's [64] equation was thus modified to the following equation by considering the effects of ultra-high strength and the steel fibers in UHPC or UHPFRC:

$$\frac{\varepsilon_c}{\varepsilon_{co}} = \left(1 + 4.3\left(\frac{f_l}{f'_{co}}\right)^{0.9}\right) \times \left\{\left[1 + 0.53\left(-\frac{\varepsilon_l}{\varepsilon_{co}}\right)\right]^{(f)} - \exp\left[-7\left(-\frac{\varepsilon_l}{\varepsilon_{co}}\right)\right]\right\} \tag{8}$$

$$f = 0.58 \times \left(\frac{f_l}{f'_{co}}\right)^{(0.1+0.5V_{sf})} + 0.3 \tag{9}$$

where f is a function of the confinement ratio f_l/f'_{co}. Eq. (8) was developed based on a regression analysis using the test results of the present study. Fig. 17 shows that the proposed equations perform much better than the original equations of Teng et al [64] in predicting the axial strain-lateral strain curves of the test specimens.

6. Conclusions

This paper presents the results of a systematic experimental program on the triaxial compression behavior of UHPC and UHPFRC by testing 32 specimens, contributing to the so far largest test database of such tests. The experimental program included the steel fiber volume fraction, the uniaxial concrete strength, and the confining pressure (ranging from 0 to 50 MPa) as the key test variables. Based on the test results, two axial stress-axial strain models and new equations for the axial strain-lateral strain relationship for UHPC and UHPFRC under various confining pressures were proposed. The results and discussions presented in the paper allow the following conclusions to be drawn:

(1) The failure patterns of UHPC and UHPFRC specimens under triaxial compression were found to be the major shear diagonal crack. An increase in confining pressure led to a smaller inclined angle (with respect to horizon) of the major shear crack.

(2) The axial stress-strain relationships of UHPC specimens under various confining pressures exhibited a sudden axial stress drop after the peak stress while the UHPFRC specimens

showed better ductility (i.e., less steep descending branch after the peak stress) especially for those with a larger confining pressure.

(3) The addition of steel fibers reduces the enhancement of peak axial stress due to a confining pressure.

(4) A residual axial stress plateau exists at the end of the descending branch of the stress-strain curve for both the UHPC and UHPFRC specimens. The presence of steel fibers increases the value of the residual axial stress.

(5) The widely used axial strain-lateral strain equation of Teng et al [64] for normal strength concrete was modified and recalibrated. The modified model provides accurate predictions for the axial strain-lateral strain curves of UHPC or UHPFRC specimens under various confining pressures.

(6) The axial stress-axial strain models were firstly proposed based on the test results in present study. The new proposed models can provide reasonably accurate predictions in terms of the peak stress, the descending branch, and the residual plateau of the test specimens.

The proposed axial stress-axial strain models and the axial strain-lateral strain equation were developed based only on limited test data; their accuracy needs to be further verified when more test data on UHPC/UHPFRC with wider ranges of concrete strength and steel fiber volume fraction become available in the future.

Acknowledgments

The authors are grateful for the financial support received from the National Natural Science Foundation of China (Project No. 52078231), the Key Research and Development Program of Hubei Province of China (Project No. 2021BCA150), and the Hong Kong Research Grants Council (Project No. T22-502/18-R).

References

[1] Shi C, Wu Z, Xiao J, Wang D, Huang Z, Fang Z. A review on ultra high performance

concrete: Part I. Raw materials and mixture design. Construction and Building Materials 2015;101:741–51. https://doi.org/10.1016/j.conbuildmat.2015.10.088.

[2] Yoo D-Y, Banthia N. Mechanical properties of ultra-high-performance fiber-reinforced concrete: A review. Cement and Concrete Composites 2016;73:267–80. https://doi.org/10.1016/j.cemconcomp.2016.08.001.

[3] Xue J, Briseghella B, Huang F, Nuti C, Tabatabai H, Chen B. Review of ultra-high performance concrete and its application in bridge engineering. Construction and Building Materials 2020;260:119844. https://doi.org/10.1016/j.conbuildmat.2020.119844.

[4] Yu R, Spiesz P, Brouwers HJH. Mix design and properties assessment of Ultra-High Performance Fibre Reinforced Concrete (UHPFRC). Cement and Concrete Research 2014;56:29–39. https://doi.org/10.1016/j.cemconres.2013.11.002.

[5] Huang B-T, Wang Y-T, Wu J-Q, Yu J, Dai J-G, Leung CK. Effect of fiber content on mechanical performance and cracking characteristics of ultra-high-performance seawater sea-sand concrete (UHP-SSC). Advances in Structural Engineering 2021;24:1182–95. https://doi.org/10.1177/1369433220972452.

[6] Wille K, Boisvert-Cotulio C. Material efficiency in the design of ultra-high performance concrete. Construction and Building Materials 2015;86:33–43. https://doi.org/10.1016/j.conbuildmat.2015.03.087.

[7] Teng J-G, Xiang Y, Yu T, Fang Z. Development and mechanical behaviour of ultra-high-performance seawater sea-sand concrete. Advances in Structural Engineering 2019;22:3100–20. https://doi.org/10.1177/1369433219858291.

[8] Akeed MH, Qaidi S, Ahmed HU, Faraj RH, Mohammed AS, Emad W, et al. Ultra-high-performance fiber-reinforced concrete. Part II: Hydration and microstructure. Case Studies in Construction Materials 2022;17:e01289. https://doi.org/10.1016/j.cscm.2022.e01289.

[9] Hassan AMT, Mahmud GH, Mohammed AS, Jones SW. The influence of normal curing temperature on the compressive strength development and flexural tensile behaviour of UHPFRC with vipulanandan model quantification. Structures 2021;30:949–59. https://doi.org/10.1016/j.istruc.2021.01.063.

[10] Emad W, Mohammed AS, Bras A, Asteris PG, Kurda R, Muhammed Z, et al. Metamodel techniques to estimate the compressive strength of UHPFRC using various mix proportions and a high range of curing temperatures. Construction and Building Materials 2022;349:128737. https://doi.org/10.1016/j.conbuildmat.2022.128737.

[11] Hassan AMT, Jones SW, Mahmud GH. Experimental test methods to determine the uniaxial tensile and compressive behaviour of ultra high performance fibre reinforced concrete (UHPFRC). Construction and Building Materials 2012;37:874–82. https://doi.org/10.1016/j.conbuildmat.2012.04.030.

[12] Graybeal BA. Compressive Behavior of Ultra-High-Performance Fiber-Reinforced Concrete. MJ 2007;104. https://doi.org/10.14359/18577.

[13] Yoo D-Y, Lee J-H, Yoon Y-S. Effect of fiber content on mechanical and fracture properties of ultra high performance fiber reinforced cementitious composites. Composite Structures 2013;106:742–53. https://doi.org/10.1016/j.compstruct.2013.07.033.

[14] Wu Z, Shi C, He W, Wu L. Effects of steel fiber content and shape on mechanical properties of ultra high performance concrete. Construction and Building Materials 2016;103:8–14. https://doi.org/10.1016/j.conbuildmat.2015.11.028.

[15] Su Y, Li J, Wu C, Wu P, Li Z-X. Effects of steel fibres on dynamic strength of UHPC. Construction and Building Materials 2016;114:708–18. https://doi.org/10.1016/j.conbuildmat.2016.04.007.

[16] Yang SL, Millard SG, Soutsos MN, Barnett SJ, Le TT. Influence of aggregate and curing regime on the mechanical properties of ultra-high performance fibre reinforced concrete (UHPFRC). Construction and Building Materials 2009;23:2291–8. https://doi.org/10.1016/j.conbuildmat.2008.11.012.

[17] Prem PR, Ramachandra Murthy A, Bharatkumar BH. Influence of curing regime and steel fibres on the mechanical properties of UHPC. Magazine of Concrete Research 2015;67:988–1002. https://doi.org/10.1680/macr.14.00333.

[18] Gesoglu M, Güneyisi E, Muhyaddin GF, Asaad DS. Strain hardening ultra-high performance fiber reinforced cementitious composites: Effect of fiber type and

concentration. Composites Part B: Engineering 2016;103:74–83. https://doi.org/10.1016/j.compositesb.2016.08.004.

[19] Liao J, Yang KY, Zeng J-J, Quach W-M, Ye Y-Y, Zhang L. Compressive behavior of FRP-confined ultra-high performance concrete (UHPC) in circular columns. Engineering Structures 2021;249:113246. https://doi.org/10.1016/j.engstruct.2021.113246.

[20] Ma K, Ma Y, Xing G, Liu B. Behavior of ultra-high-performance concrete columns subjected to axial compressive load. Advances in Structural Engineering 2021;24:3792–808. https://doi.org/10.1177/13694332211038440.

[21] Hu R, Fang Z, Jiang R, Xiang Y, Liu C. Fatigue prediction model of ultra-high-performance concrete beams prestressed with CFRP tendons. Advances in Structural Engineering 2022;25:611–24. https://doi.org/10.1177/13694332211062340.

[22] Yang X, Zohrevand P, Mirmiran A. Behavior of Ultrahigh-Performance Concrete Confined by Steel. J Mater Civ Eng 2016;28:04016113. https://doi.org/10.1061/(ASCE)MT.1943-5533.0001623.

[23] Hoang AL, Fehling E, Lai B, Thai D-K, Chau NV. Experimental study on structural performance of UHPC and UHPFRC columns confined with steel tube. Engineering Structures 2019;187:457–77. https://doi.org/10.1016/j.engstruct.2019.02.063.

[24] Zohrevand P, Mirmiran A. Behavior of Ultrahigh-Performance Concrete Confined by Fiber-Reinforced Polymers. J Mater Civ Eng 2011;23:1727–34. https://doi.org/10.1061/(ASCE)MT.1943-5533.0000324.

[25] Tian H, Zhou Z, Wei Y, Wang Y, Lu J. Experimental investigation on axial compressive behavior of ultra-high performance concrete (UHPC) filled glass FRP tubes. Construction and Building Materials 2019;225:678–91. https://doi.org/10.1016/j.conbuildmat.2019.07.204.

[26] Guler S. Axial behavior of FRP-wrapped circular ultra-high performance concrete specimens. Structural Engineering and Mechanics 2014;50:709–22. https://doi.org/10.12989/SEM.2014.50.6.709.

[27] Wang W, Wu C, Liu Z, Si H. Compressive behavior of ultra-high performance fiber-

reinforced concrete (UHPFRC) confined with FRP. Composite Structures 2018;204:419–37. https://doi.org/10.1016/j.compstruct.2018.07.102.

[28] Lam L, Huang L, Xie J-H, Chen J-F. Compressive behavior of ultra-high performance concrete confined with FRP. Composite Structures 2021;274:114321. https://doi.org/10.1016/j.compstruct.2021.114321.

[29] Xiao QG, Teng JG, Yu T. Behavior and Modeling of Confined High-Strength Concrete. J Compos Constr 2010;14:249–59. https://doi.org/10.1061/(ASCE)CC.1943-5614.0000070.

[30] Gholampour A, Ozbakkaloglu T. Fiber-reinforced concrete containing ultra high-strength micro steel fibers under active confinement. Construction and Building Materials 2018;187:299–306. https://doi.org/10.1016/j.conbuildmat.2018.07.042.

[31] fib (International Federation for Structural Concrete) 2013. fib Model Code for concrete structures. Berlin: Ernst & Sohn GmbH & Co KG 2013.

[32] ABNT (Associação Brasileira de Normas Técnicas) 2014. Design of concrete structures—Procedure. ABNT NBR 6118 Rio de Janeiro, Brazil: ABNT 2014.

[33] ASTM C1856/C1856M. Standard Practice for Fabricating and Testing Specimens of Ultra-High Performance Concrete. American Society for Testing and Materials 2017.

[34] CSA-A23.1. Annex U of ‘Ultra-High-Performance Concrete.’ Canadian Standards Association 2019.

[35] Richart FE, Brandtzaeg A, Brown RL. A study of the failure of concrete under combined compressive stresses. Bulletin No185, Univ of Illinois, Engineering Experimental Station, Champaign, IL 1928.

[36] Sfer D, Carol I, Gettu R, Etse G. Study of the Behavior of Concrete under Triaxial Compression. J Eng Mech 2002;128:156–63. https://doi.org/10.1061/(ASCE)0733-9399(2002)128:2(156).

[37] Sheikh SA, Laine D, Cui C. Behavior of Normal- and High-Strength Confined Concrete. ACI Structural Journal 2013;110:989–99.

[38] Candappa DC, Sanjayan JG, Setunge S. Complete Triaxial Stress-Strain Curves of High-Strength Concrete. J Mater Civ Eng 2001;13:209–15.

https://doi.org/10.1061/(ASCE)0899-1561(2001)13:3(209).

[39] Attard MM, Setunge S. Stress-Strain Relationship of Confined and Unconfined Concrete. ACI Materials Journal 1996;93. https://doi.org/10.14359/9847.

[40] Ansari F, Li Q. High-Strength Concrete Subjected to Triaxial Compression. ACI Materials Journal 1998;95. https://doi.org/10.14359/420.

[41] Xie J, Elwi AE, MacGregor JG. Mechanical Properties of Three High-Strength Concretes Containing Silica Fume. ACI Materials Journal 1995;92. https://doi.org/10.14359/9764.

[42] Li Q, Ansari F. High-Strength Concrete in Triaxial Compression by Different Sizes of Specimens. ACI Materials Journal 2000;97:684–9.

[43] Li Q, Ansari F. Mechanics of Damage and Constitutive Relationships for High-Strength Concrete in Triaxial Compression. Journal of Engineering Mechanics 1999;125:1–10. https://doi.org/10.1061/(ASCE)0733-9399(1999)125:1(1).

[44] Lu X, Hsu C-TT. Behavior of high strength concrete with and without steel fiber reinforcement in triaxial compression. Cement and Concrete Research 2006;36:1679–85. https://doi.org/10.1016/j.cemconres.2006.05.021.

[45] Farnam Y, Moosavi M, Shekarchi M, Babanajad SK, Bagherzadeh A. Behaviour of Slurry Infiltrated Fibre Concrete (SIFCON) under triaxial compression. Cement and Concrete Research 2010;40:1571–81. https://doi.org/10.1016/j.cemconres.2010.06.009.

[46] Babanajad SK, Farnam Y, Shekarchi M. Failure criteria and triaxial behaviour of HPFRC containing high reactivity metakaolin and silica fume. Construction and Building Materials 2012;29:215–29. https://doi.org/10.1016/j.conbuildmat.2011.08.094.

[47] Wang Y-B, Liew JYR, Lee SC, Xiong DX. Experimental Study of Ultra-High-Strength Concrete under Triaxial Compression. ACI Materials Journal 2016;113. https://doi.org/10.14359/51688071.

[48] Zhang K, Zhao L-Y, Ni T, Zhu Q-Z, Shen J, Fan Y-H. Experimental investigation and multiscale modeling of reactive powder cement pastes subject to triaxial compressive stresses. Construction and Building Materials 2019;224:242–54. https://doi.org/10.1016/j.conbuildmat.2019.07.049.

[49] Wu L, Wang Z, Liu D, Zhu H, Lu Y, Lin L. Effect of Confining Pressure and Steel Fiber Volume Content on Mechanical Property of Reactive Powder Concrete. Journal of Building Materials 2018;21:208–15.

[50] Vogel F, Sovják R, Jogl M. Experimental Tests of the UHPC in Triaxial Compression. Applied Mechanics and Materials 2013;486:78–83. https://doi.org/10.4028/www.scientific.net/AMM.486.78.

[51] Wang Y-Z, Wang Y-B, Zhao Y-Z, Li G-Q, Lyu Y-F, Li H. Experimental study on ultra-high performance concrete under triaxial compression. Construction and Building Materials 2020;263:120225. https://doi.org/10.1016/j.conbuildmat.2020.120225.

[52] Wu P, Wu C, Liu Z, Xu S, Li J, Li J. Triaxial strength and failure criterion of ultra-high performance concrete. Advances in Structural Engineering 2022:136943322210806. https://doi.org/10.1177/13694332221080603.

[53] ASTM C469/C469M. Standard Test Method for Static Modulus of Elasticity and Poisson's Ratio of Concrete in Compression. American Society for Testing and Materials 2002.

[54] Mirmiran A, Shahawy M. Dilation characteristics of confined concrete. Mech Cohes-Frict Mater 1997;2:237–49. https://doi.org/10.1002/(SICI)1099-1484(199707)2:3<237::AID-CFM32>3.0.CO;2-2.

[55] Popovics S. A numerical approach to the complete stress-strain curve of concrete. Cement and Concrete Research 1973;3:583–99. https://doi.org/10.1016/0008-8846(73)90096-3.

[56] Fam A, Rizkalla SH. Confinement Model for Axially Loaded Concrete Confined by Circular Fiber-Reinforced Polymer Tubes. Aci Structural Journal 2001;98:451–61.

[57] Marques SPC, Marques DC dos SC, Lins da Silva J, Cavalcante MAA. Model for Analysis of Short Columns of Concrete Confined by Fiber-Reinforced Polymer. J Compos Constr 2004;8:332–40. https://doi.org/10.1061/(ASCE)1090-0268(2004)8:4(332).

[58] Binici B. An analytical model for stress–strain behavior of confined concrete. Engineering Structures 2005;27:1040–51. https://doi.org/10.1016/j.engstruct.2005.03.002.

[59] Jiang T, Teng JG. Analysis-oriented stress–strain models for FRP–confined concrete. Engineering Structures 2007;29:2968–86. https://doi.org/10.1016/j.engstruct.2007.01.010.

[60] Lim JC, Ozbakkaloglu T. Stress–strain model for normal- and light-weight concretes under uniaxial and triaxial compression. Construction and Building Materials 2014;71:492–509. https://doi.org/10.1016/j.conbuildmat.2014.08.050.

[61] Imran I, Pantazopoulou SJ. Plasticity Model for Concrete under Triaxial Compression. J Eng Mech 2001;127:281–90. https://doi.org/10.1061/(ASCE)0733-9399(2001)127:3(281).

[62] Shawn S. Smith, Kasper J. Willam, Kurt H. Gerstle, Stein Sture. Concrete Over the Top--Or, is there Life After Peak? ACI Materials Journal n.d.;86.

[63] Samani AK, Attard MM. A stress–strain model for uniaxial and confined concrete under compression. Engineering Structures 2012;41:335–49. https://doi.org/10.1016/j.engstruct.2012.03.027.

[64] Teng JG, Huang YL, Lam L, Ye LP. Theoretical Model for Fiber-Reinforced Polymer-Confined Concrete. J Compos Constr 2007;11:201–10. https://doi.org/10.1061/(ASCE)1090-0268(2007)11:2(201).

Table 1 Experimental program of triaxial compression tests

Specimen	Concrete grade	Steel fiber volume fraction (%)	Confining pressure (MPa)	No. of identical specimens
UHPC-1-0	1	0	0	1
UHPC-1-10-1,2	1	0	10	2
UHPC-1-30-1,2	1	0	30	2
UHPC-1-50-1,2	1	0	50	2
UHPC-2-0	2	0	0	1
UHPC-2-10-1,2	2	0	10	2
UHPC-2-30-1,2	2	0	30	2
UHPC-2-50-1,2	2	0	50	2
UHPFRC-1-0	1	2	0	1
UHPFRC-1-10-1,2	1	2	10	2
UHPFRC-1-20-1,2	1	2	20	2
UHPFRC-1-30-1,2	1	2	30	2
UHPFRC-1-40-1,2	1	2	40	2
UHPFRC-1-50-1,2	1	2	50	2
UHPFRC-2-0	2	2	0	1
UHPFRC-2-10-1,2	2	2	10	2
UHPFRC-2-30-1,2	2	2	30	2
UHPFRC-2-50-1,2	2	2	50	2

Table 2 Properties of steel fibers

Cross-section	Fiber type	Diameter (mm)	Length (mm)	Aspect ratio	Tensile strength (MPa)
Circle	Straight	0.2	13	65	>2600

Table 3 Mix proportions of UHPC and UHPFRC (kg/m^3)

Series	Cement	Silica fume	Fly ash	Quartz sand	Quartz powder	Steel fiber	Superplasticizer	Water
UHPC-1	800	240	112	960	224	0	40	208
UHPC-2	800	240	112	960	224	0	36	240
UHPFRC-1	800	240	112	960	224	156	40	208
UHPFRC-2	800	240	112	960	224	156	36	240

Table 4 Uniaxial compression test results

Specimen	Diameter (mm)	Height (mm)	Compressive strength (MPa)	Axial strain at peak stress (%)	Elastic modulus (GPa)
UHPC-1	100	200	129.2	0.324	40.5
UHPC-2	100	200	113.4	0.287	45.1
UHPFRC-1	100	200	164.5	0.427	39.3
UHPFRC-2	100	200	139.1	0.398	36.6
UHPC-1	50	100	126.9	0.318	44.5
UHPC-2	50	100	101.0	0.269	46.6
UHPFRC-1	50	100	151.5	0.435	40.1
UHPFRC-2	50	100	127.1	0.423	38.3

Table 5 Triaxial compression test results

Specimen	f_{cc} (MPa)	ε_{cc} (%)	f_l (MPa)	f_l/f'_{co}	f_{cc}/f'_{co}	$\varepsilon_{cc}/\varepsilon_{co}$	f_{cres} (MPa)
UHPC-1-0	126.92	0.32	0	0.00	1.00	1.00	—
UHPC-1-10-1	187.41	0.66	10	0.08	1.48	2.08	—
UHPC-1-10-2	173.97	0.65	10	0.08	1.37	2.05	—
UHPC-1-30-1	233.55	1.08	30	0.24	1.84	3.40	154.08
UHPC-1-30-2	257.72	1.22	30	0.24	2.03	3.82	140.05
UHPC-1-50-1	292.87	1.05	50	0.39	2.31	3.30	—
UHPC-1-50-2	331.91	1.74	50	0.39	2.62	5.46	270.01
UHPC-2-0	101.03	0.27	0	0.00	1.00	1.00	—
UHPC-2-10-1	128.06	0.54	10	0.10	1.27	1.99	—
UHPC-2-10-2	156.76	0.56	10	0.10	1.55	2.10	—
UHPC-2-30-1	216.58	1.11	30	0.30	2.14	4.14	140.77
UHPC-2-30-2	217.81	1.07	30	0.30	2.16	3.96	126.43
UHPC-2-50-1	241.59	0.67	50	0.49	2.39	2.49	—
UHPC-2-50-2	290.14	1.69	50	0.49	2.87	6.26	241.43
UHPFRC-1-0	151.46	0.44	0	0.00	1.00	1.00	—
UHPFRC-1-10-1	188.54	0.73	10	0.07	1.24	1.67	—
UHPFRC-1-10-2	195.14	0.72	10	0.07	1.29	1.65	—
UHPFRC-1-20-1	237.87	1.09	20	0.13	1.57	2.51	127.62
UHPFRC-1-20-2	210.51	0.99	20	0.13	1.39	2.27	105.68
UHPFRC-1-30-1	246.87	1.38	30	0.20	1.63	3.17	172.08
UHPFRC-1-30-2	252.39	1.40	30	0.20	1.67	3.21	147.38
UHPFRC-1-40-1	281.55	1.96	40	0.26	1.86	4.51	231.63
UHPFRC-1-40-2	277.71	2.01	40	0.26	1.83	4.61	209.75
UHPFRC-1-50-1	315.52	2.36	50	0.33	2.08	5.43	284.88
UHPFRC-1-50-2	303.40	2.32	50	0.33	2.00	5.33	—
UHPFRC-2-0	127.10	0.42	0	0.00	1.00	1.00	—
UHPFRC-2-10-1	152.18	0.73	10	0.08	1.20	1.73	—
UHPFRC-2-10-2	154.82	0.78	10	0.08	1.22	1.83	—
UHPFRC-2-30-1	214.95	2.00	30	0.24	1.69	4.71	142.32
UHPFRC-2-30-2	198.02	1.87	30	0.24	1.56	4.42	158.02
UHPFRC-2-50-1	309.40	3.05	50	0.39	2.43	7.20	256.84
UHPFRC-2-50-2	289.87	2.80	50	0.39	2.28	6.61	300.13

Note: "—" is not applicable according to the definition in present study.

Table 6 Triaxial compression tests of UHPC/UHPFRC specimens from literature

Number	Diameter (mm)	Height (mm)	V_{sf} (%)	f'_{co} (MPa)	ε_{co} (%)	f_l (MPa)	f_{cc} (MPa)	ε_{cc} (%)	f_{cres} (MPa)
Zhang et al. [48]									
1	50	100	0	184	NA	5	239	0.97	—
2	50	100	0	184	NA	10	271	1.06	—
3	50	100	0	184	NA	20	294	1.37	—
4	50	100	0	184	NA	30	327	1.65	—
5	50	100	0	184	NA	40	351	2.03	—
Wu et al. [49]									
6	43.6	130	0	143.15	0.47	10	234.25	NA	—
7	43.6	130	0	143.15	0.47	20	267.81	NA	—
8	43.6	130	0	143.15	0.47	40	332.53	NA	—
9	43.6	130	0	143.15	0.47	70	406.85	NA	350
10	43.6	130	0.3	152.74	0.49	10	229.45	NA	—
11	43.6	130	0.3	152.74	0.49	20	260.62	NA	169
12	43.6	130	0.3	152.74	0.49	40	332.53	NA	245
13	43.6	130	0.3	152.74	0.49	70	402.06	NA	380
14	43.6	130	1	155.14	0.49	10	225.86	NA	—
15	43.6	130	1	155.14	0.49	20	276.20	NA	—
16	43.6	130	1	155.14	0.49	40	348.12	NA	255
17	43.6	130	1	155.14	0.49	70	408.05	NA	363
18	43.6	130	1.7	164.73	0.52	10	228.25	NA	92
19	43.6	130	1.7	164.73	0.52	20	278.60	NA	147
20	43.6	130	1.7	164.73	0.52	40	343.32	NA	—
21	43.6	130	1.7	164.73	0.52	70	423.63	NA	—
22	43.6	130	2.4	159.93	0.53	10	234.25	NA	113
23	43.6	130	2.4	159.93	0.53	20	276.20	NA	—
24	43.6	130	2.4	159.93	0.53	40	333.73	NA	—
25	43.6	130	2.4	159.93	0.53	70	430.82	NA	—
Vogel et al. [50]									
26	100	200	0	122.50	NA	10	178.00	NA	NA
27	100	200	0	122.50	NA	20	208.50	NA	NA
28	100	200	0	122.50	NA	30	230.50	NA	NA
Wang et al. [51]									
29	50	100	0	125.60	0.30	5	197.00	0.51	—
30	50	100	0	125.60	0.30	10	215.90	0.58	—
31	50	100	0	125.60	0.30	20	281.70	0.84	—
32	50	100	0	125.60	0.30	30	296.40	0.84	—

33	50	100	0	125.60	0.30	40	338.80	1.30	—
34	50	100	0	125.60	0.30	50	374.80	1.63	—
35	50	100	1.5	153.40	0.34	5	186.20	0.46	—
36	50	100	1.5	153.40	0.34	10	236.00	0.67	112
37	50	100	1.5	153.40	0.34	20	276.60	0.88	—
38	50	100	1.5	153.40	0.34	30	332.70	1.10	—
39	50	100	1.5	153.40	0.34	40	352.80	1.45	—
40	50	100	1.5	153.40	0.34	50	358.10	1.81	—

Note: "—" is not applicable according to the definition in present study, "NA" is not available in the study.

Fig. 1. Surface patching using gypsum for specimens of triaxial compression tests

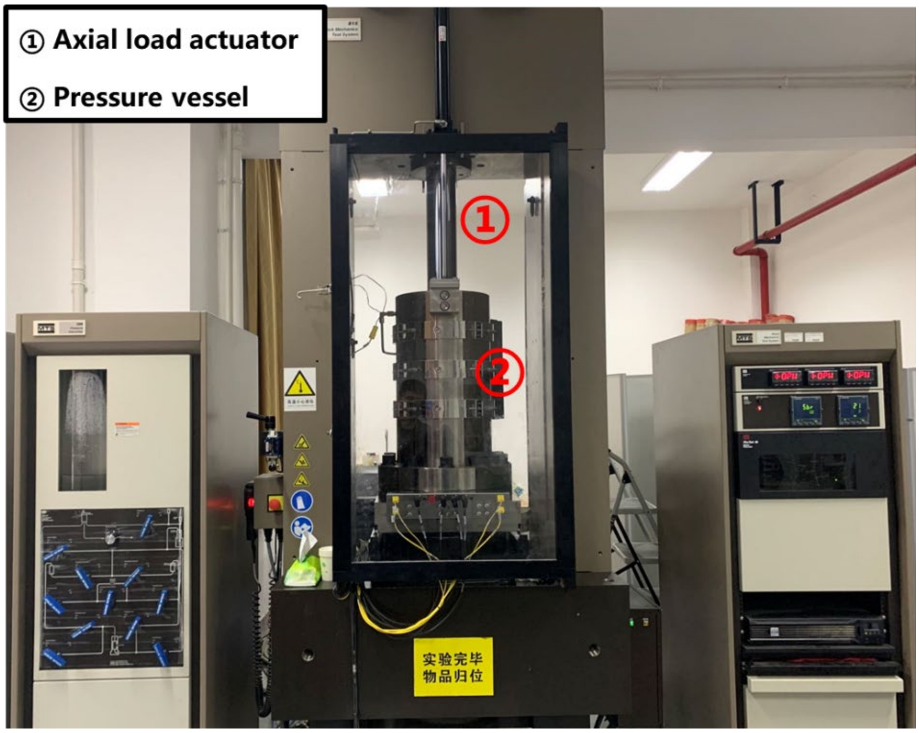

Fig. 2. Triaxial compression test system

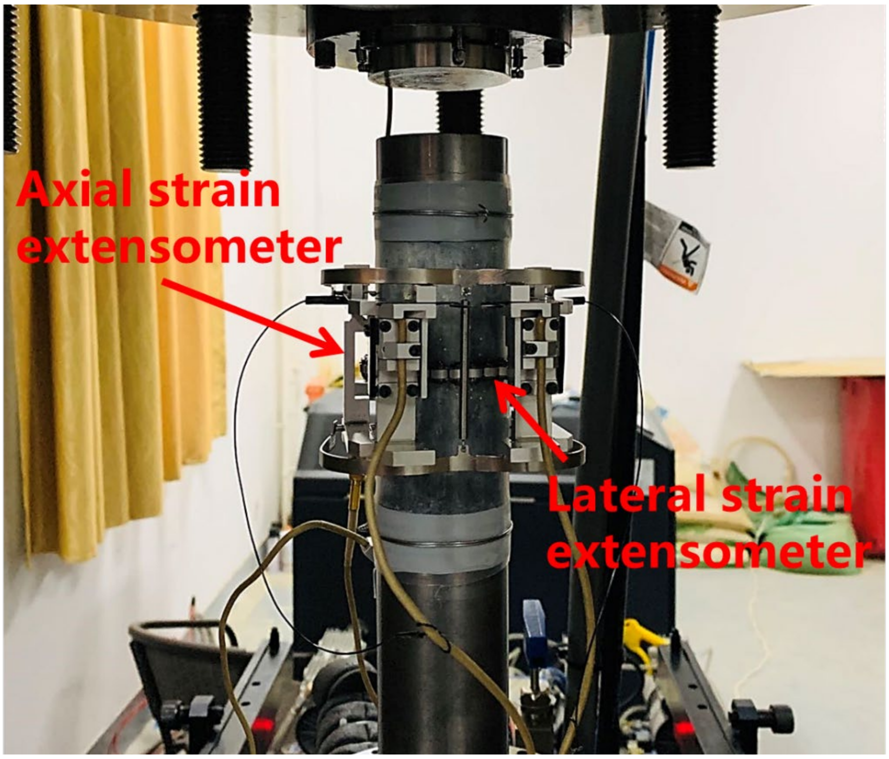

Fig. 3. Layout of axial strain and lateral strain extensometers

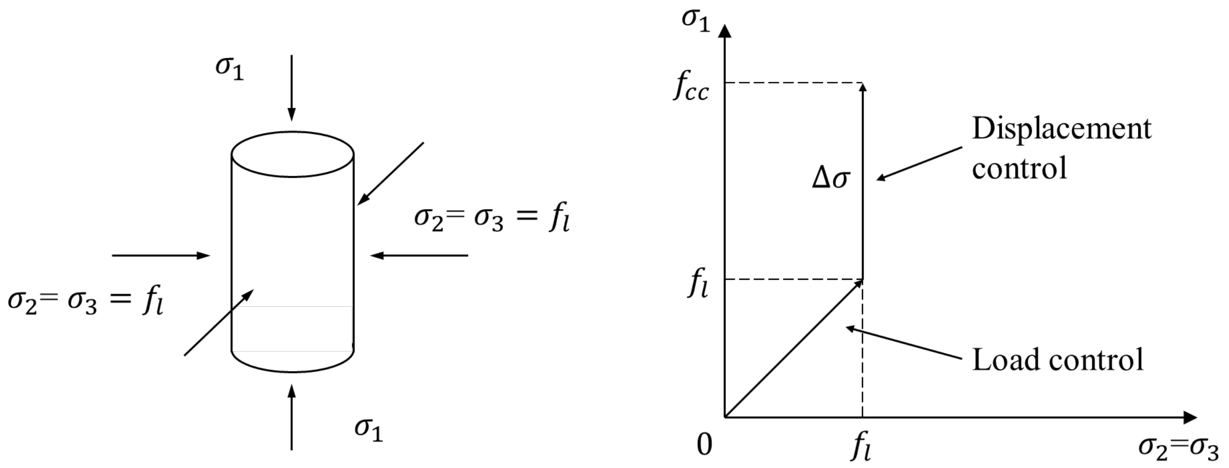

Fig. 4. Stress state of specimen and loading path of triaxial compression tests

(a) UHPC-1

(b) UHPC-2

(c) UHPFRC-1

(d) UHPFRC-2

Fig. 5. Failure modes of UHPC and UHPFRC specimens (50 mm × 100 mm) under uniaxial compression

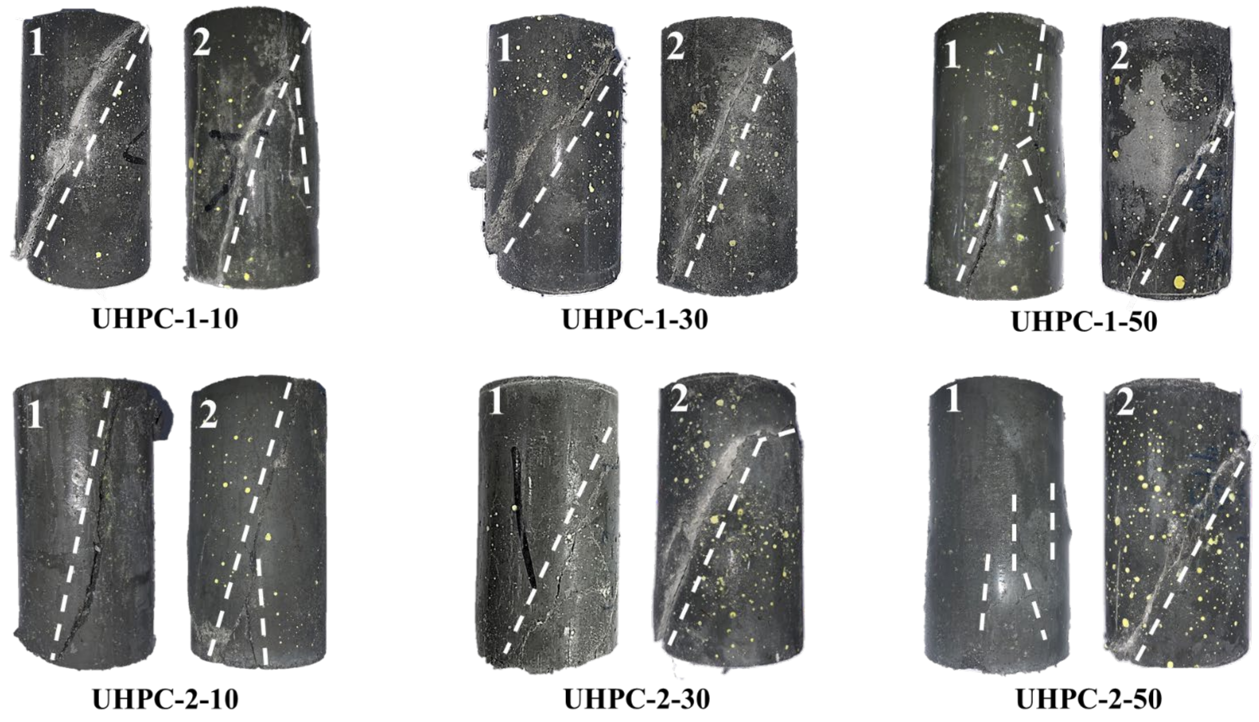
UHPC-1-10
UHPC-1-30
UHPC-1-50
UHPC-2-10
UHPC-2-30
UHPC-2-50

(a) UHPC

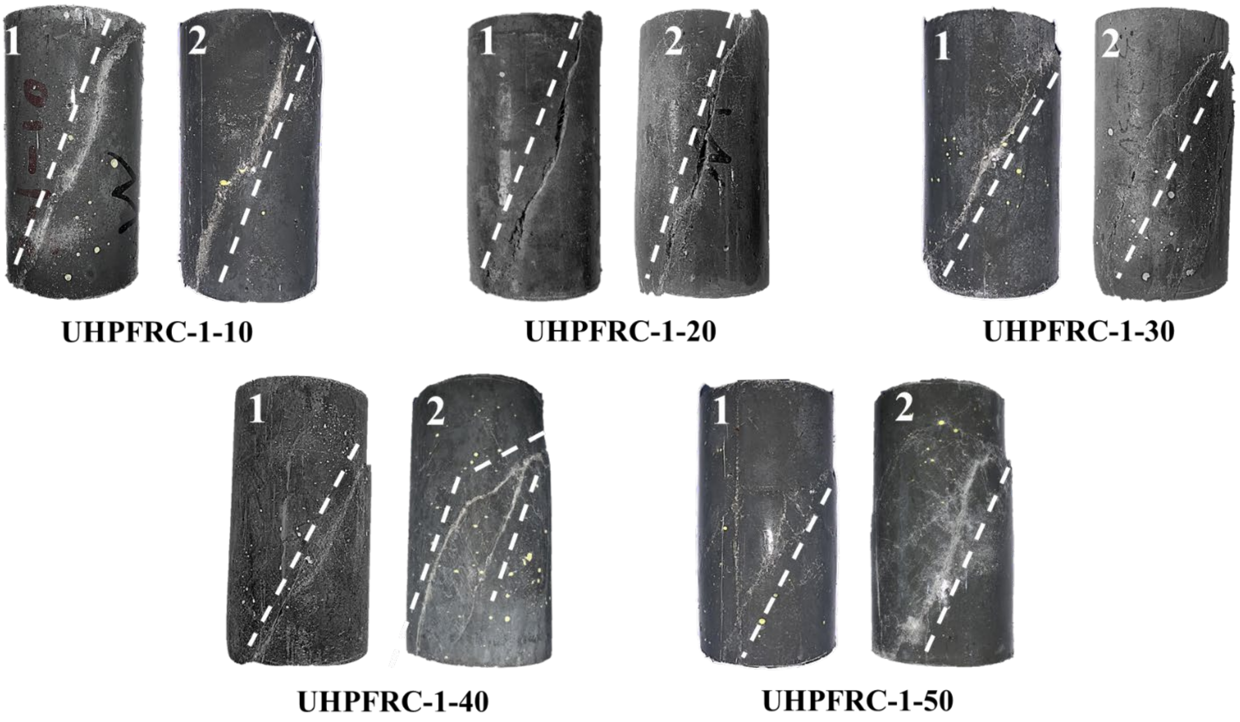
UHPFRC-1-10
UHPFRC-1-20
UHPFRC-1-30
UHPFRC-1-40
UHPFRC-1-50

UHPFRC-2-10 **UHPFRC-2-30** **UHPFRC-2-50**

(b) UHPFRC

Fig. 6. Failure modes of UHPC and UHPFRC specimens under triaxial compression

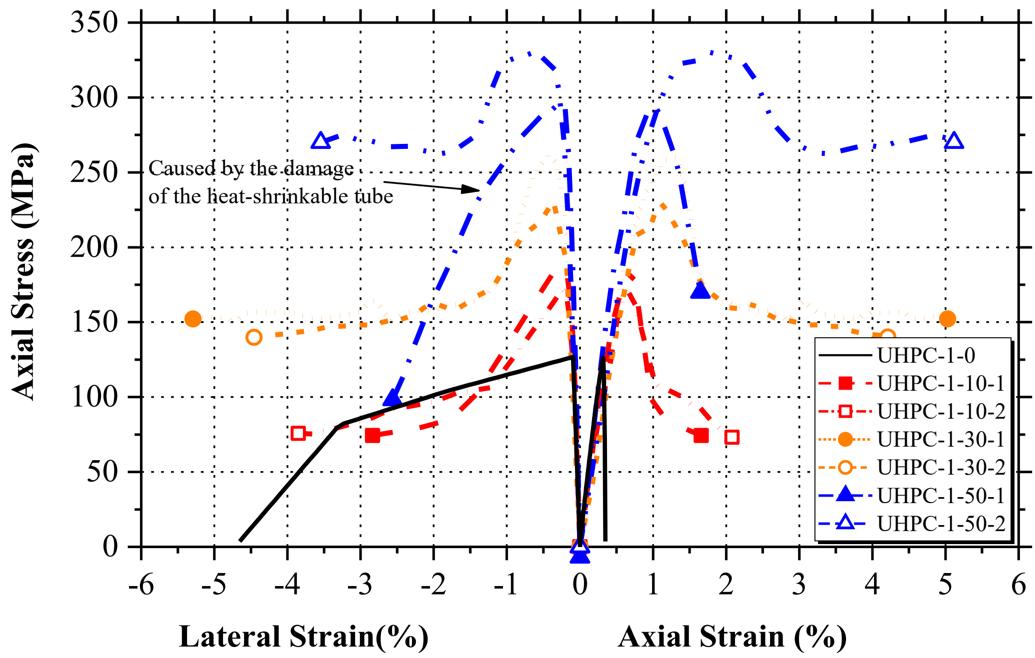

(a) UHPC-1

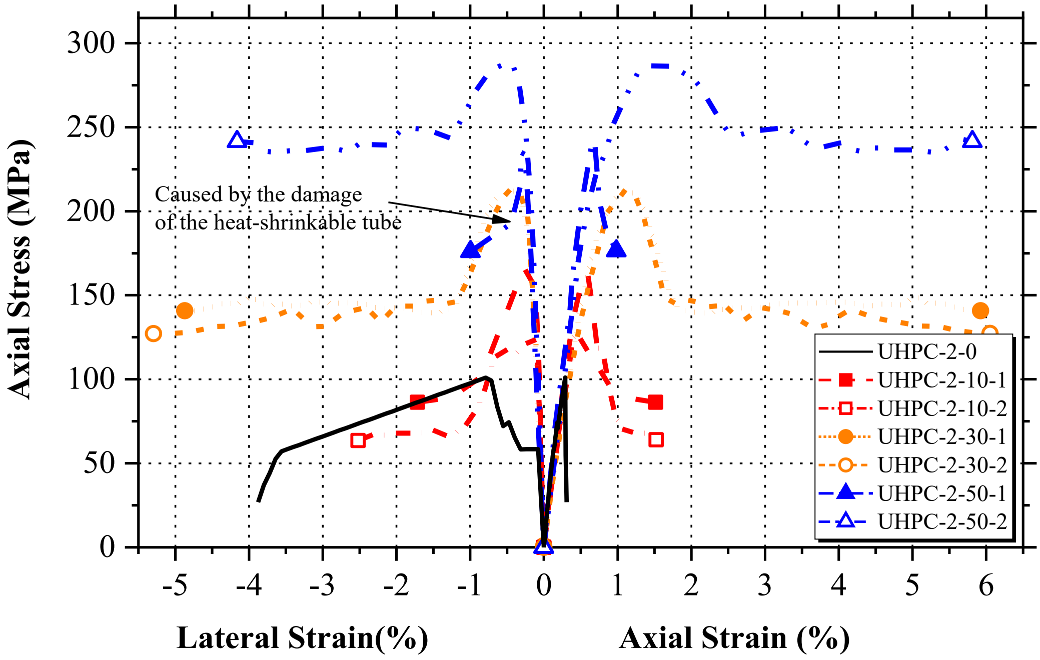

(b) UHPC-2

Fig. 7. Stress-strain curves of UHPC under different confining pressures

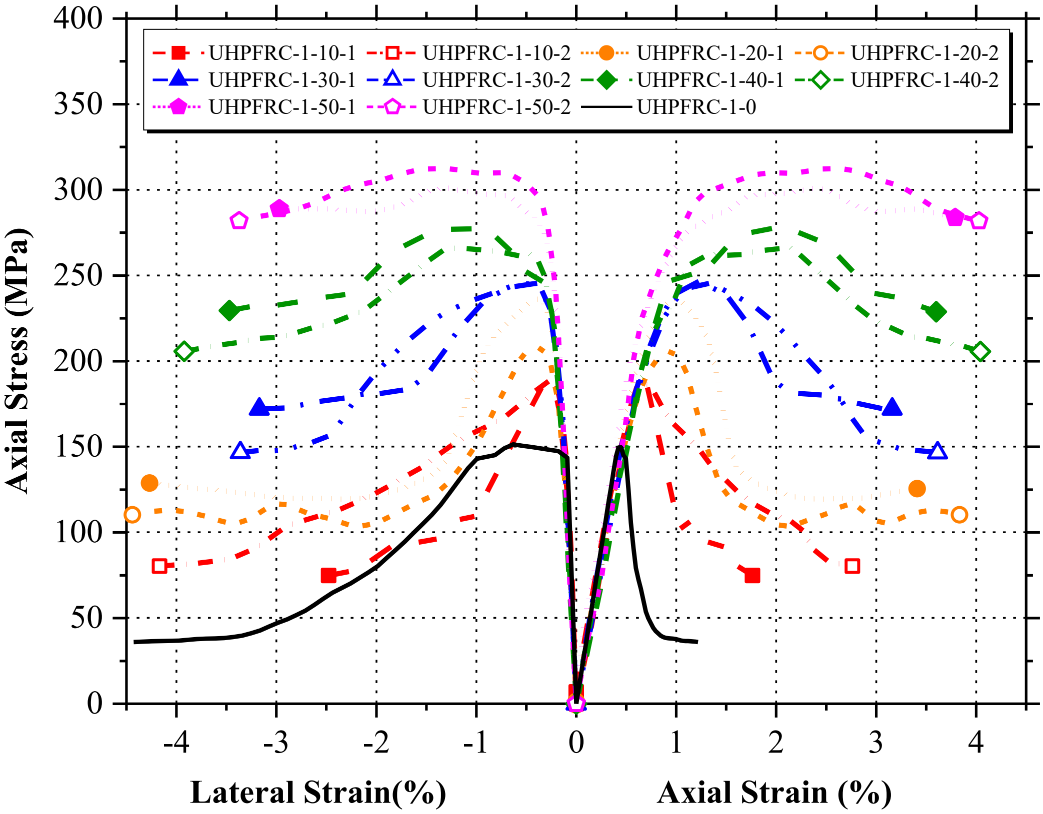

(a) UHPFRC-1

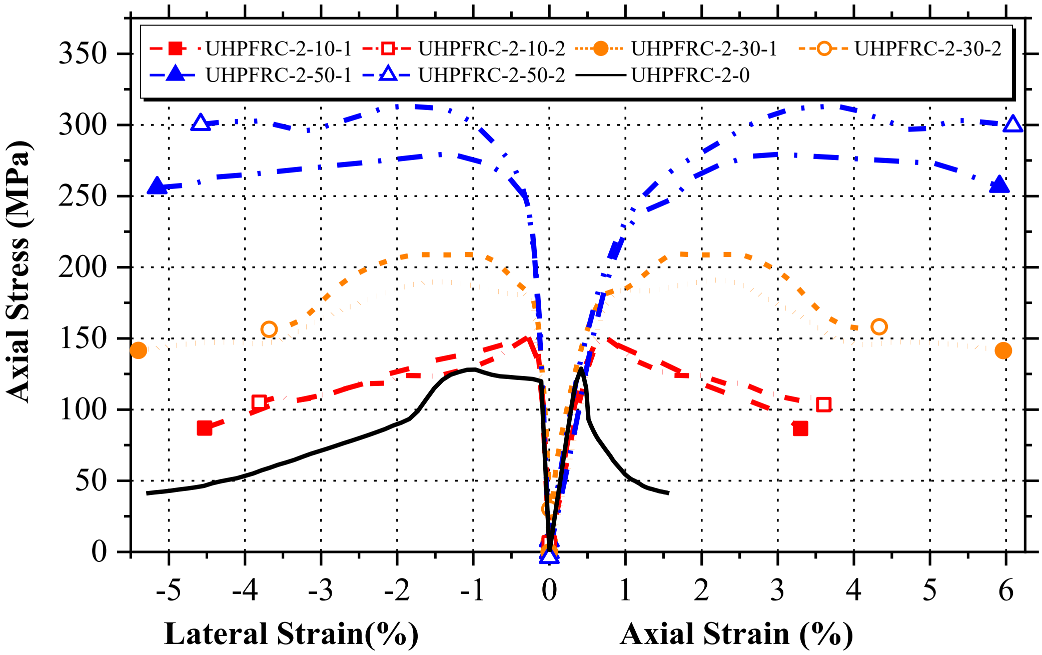

(b) UHPFRC-2

Fig. 8. Stress-strain curves of UHPFRC under different confining pressures

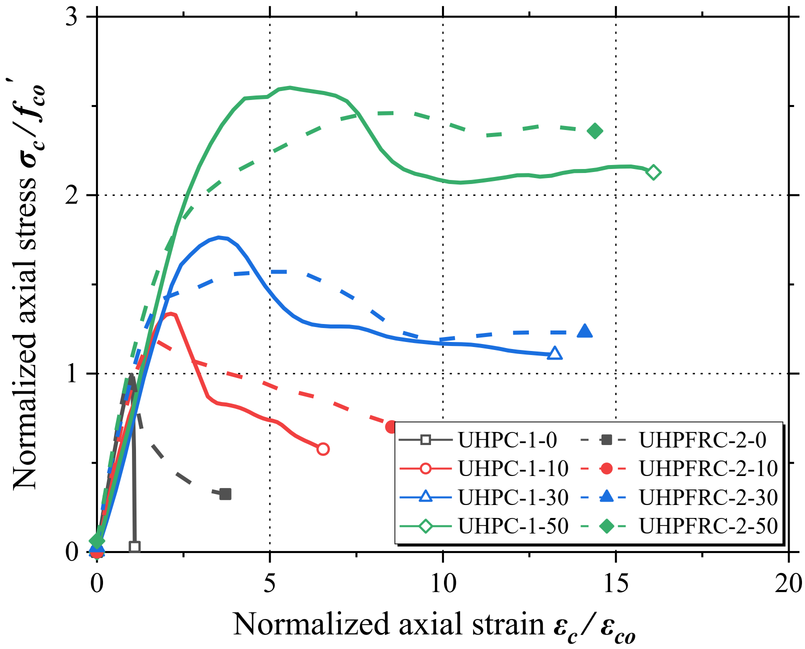

Fig. 9. Normalized axial stress−axial strain curves of UHPC and UHPFRC

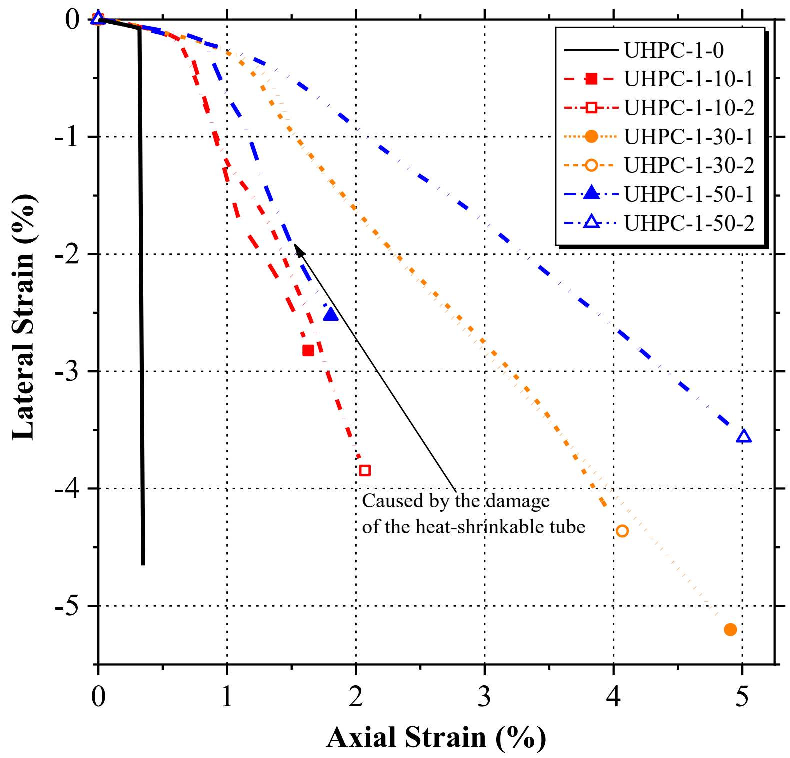

(a) UHPC-1

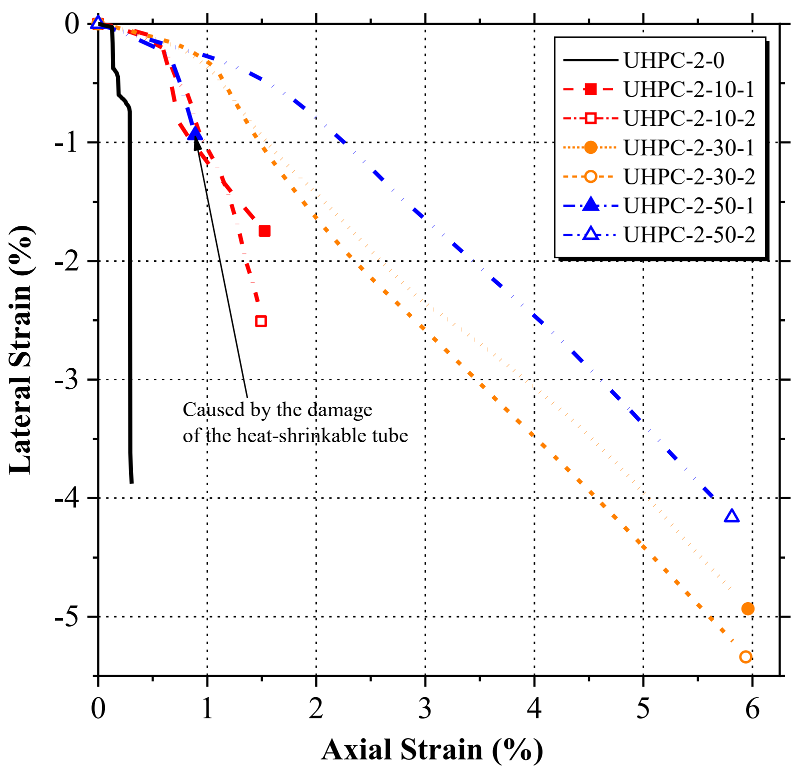

(b) UHPC-2

Fig. 10. Axial strain-lateral strain curves of UHPC specimens under different confining pressures

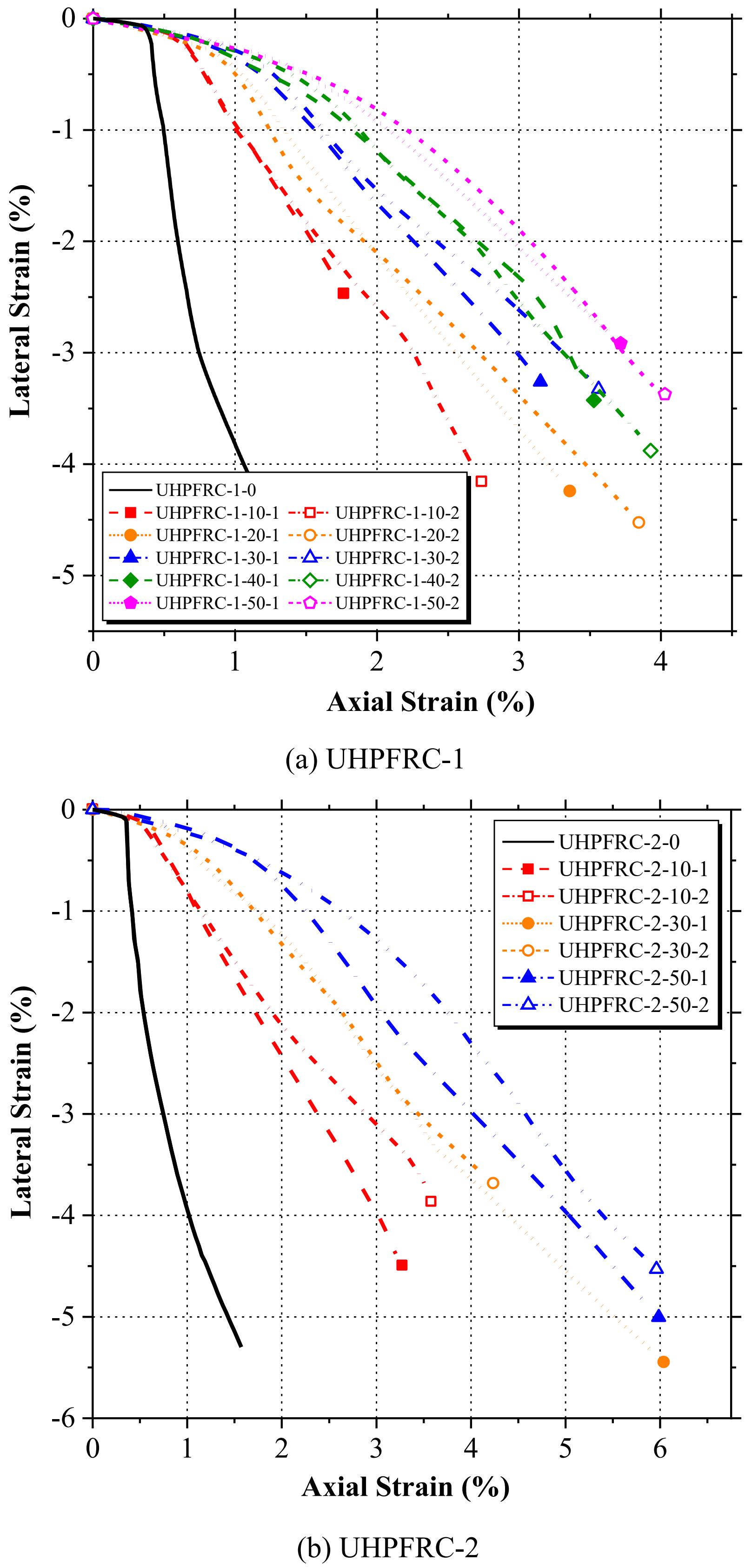

Fig. 11. Axial strain-lateral strain curves of UHPFRC specimens under different confining pressures

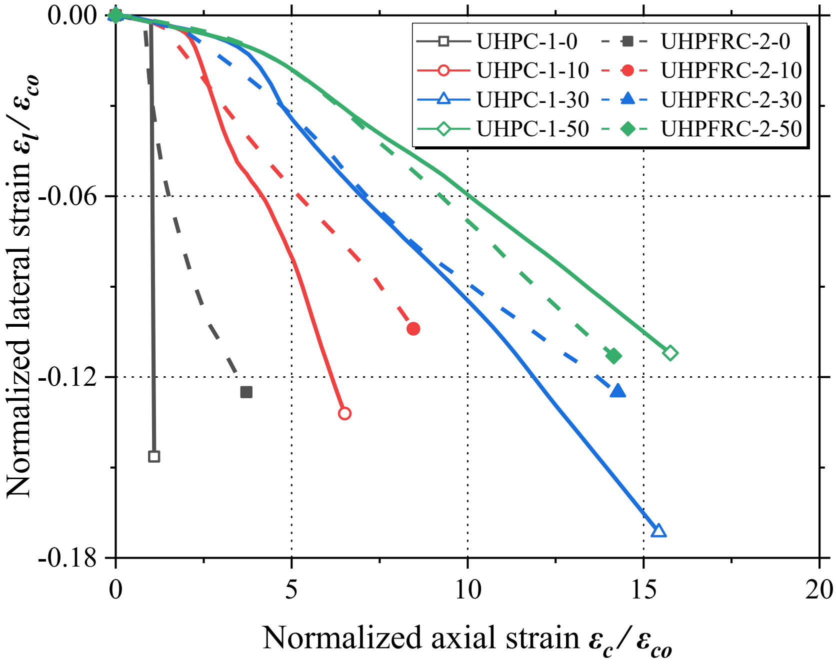

Fig. 12. Normalized axial strain-lateral strain curves of UHPC and UHPFRC

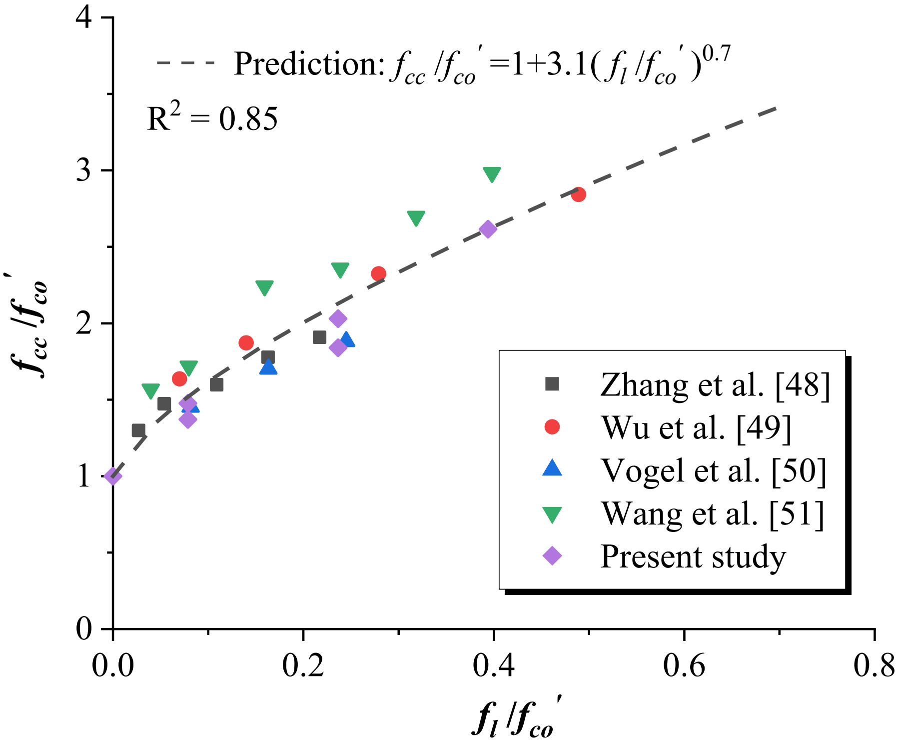

(a) UHPC

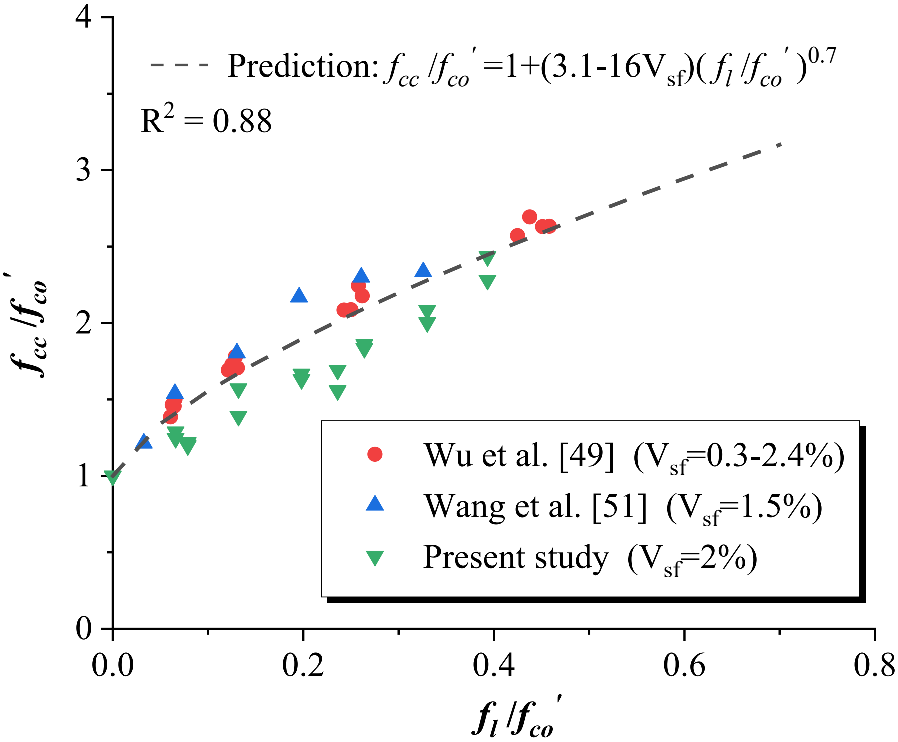

(b) UHPFRC

Fig. 13. Relationship between normalized peak axial stress f_{cc}/f_{co}' and confinement ratio f_l/f_{co}'

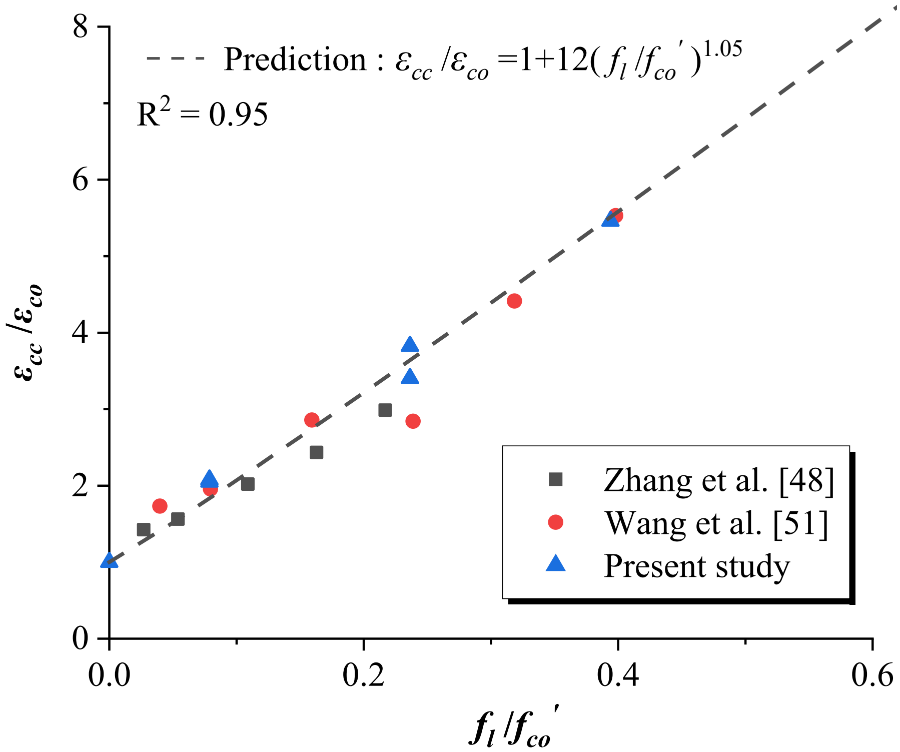

(a) UHPC

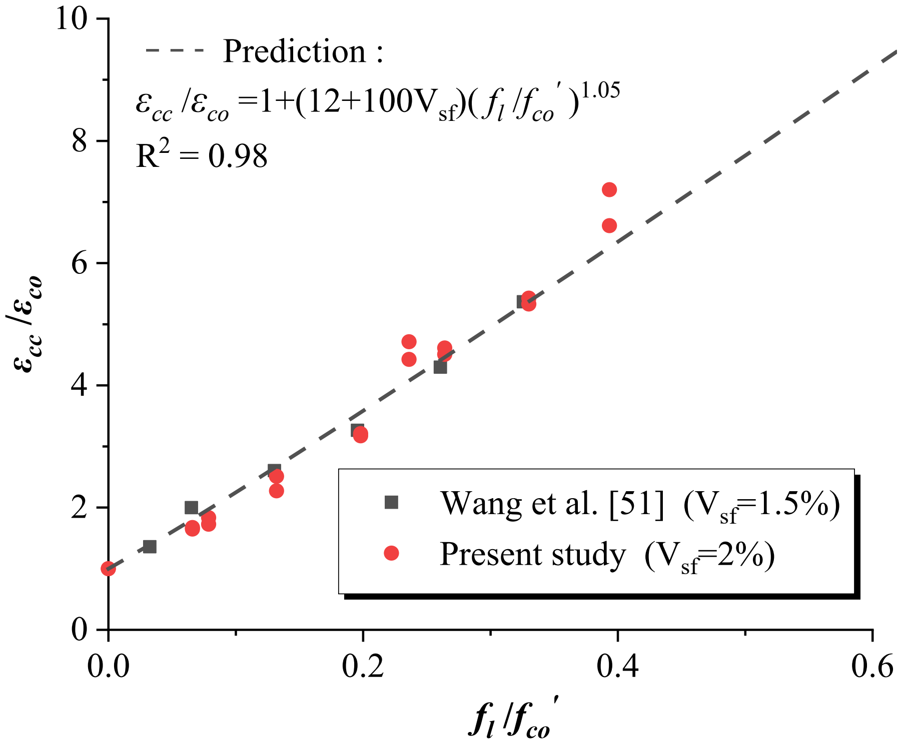

(b) UHPFRC

Fig. 14. Relationship between normalized axial strain $\varepsilon_{cc}/\varepsilon_{co}$ and confinement ratio f_l/f_{co}'

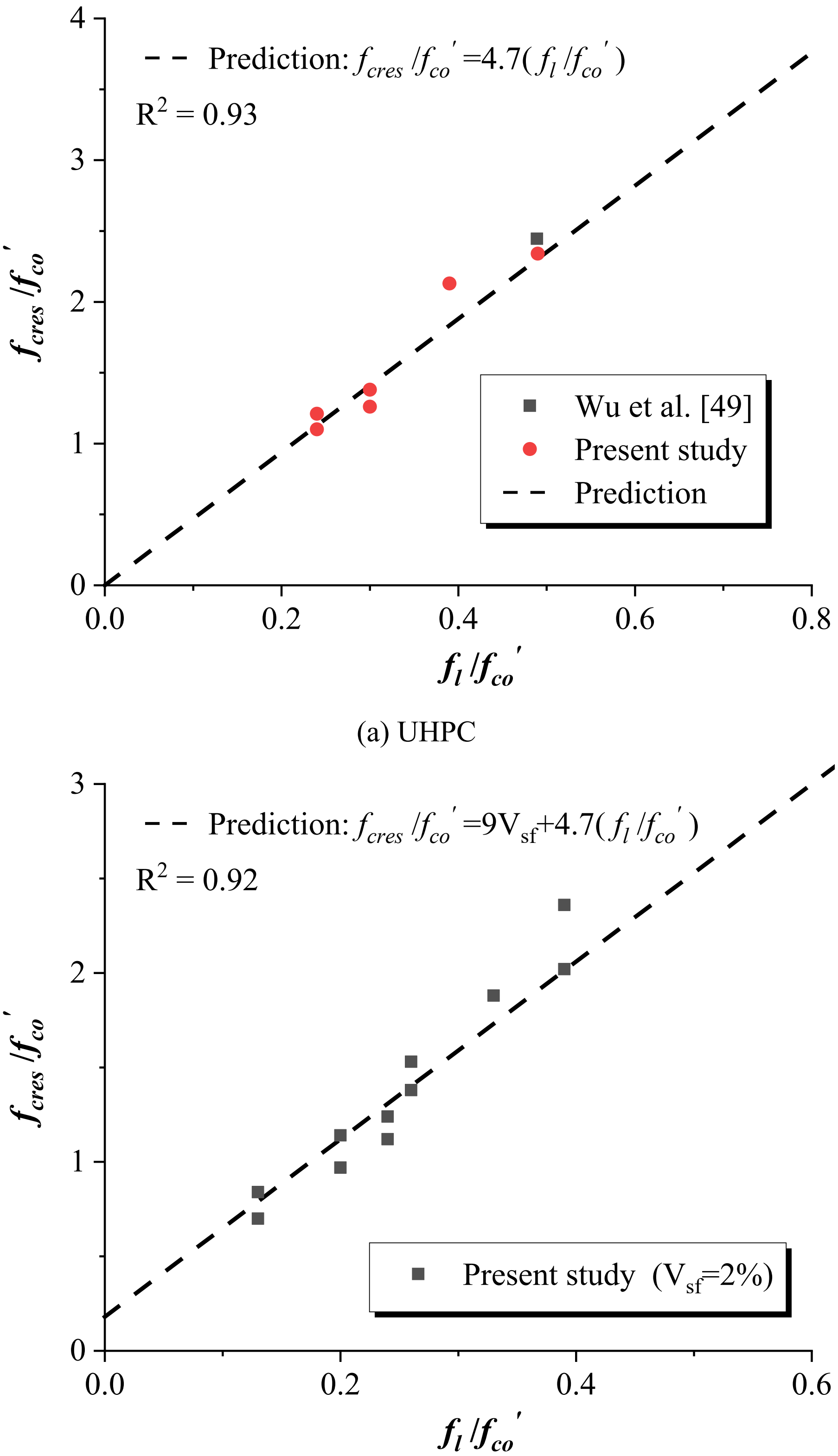

(a) UHPC

(b) UHPFRC

Fig. 15. Relationship between normalized residual axial stress f_{cres}/f'_{co} and confinement ratio f_l/f'_{co}

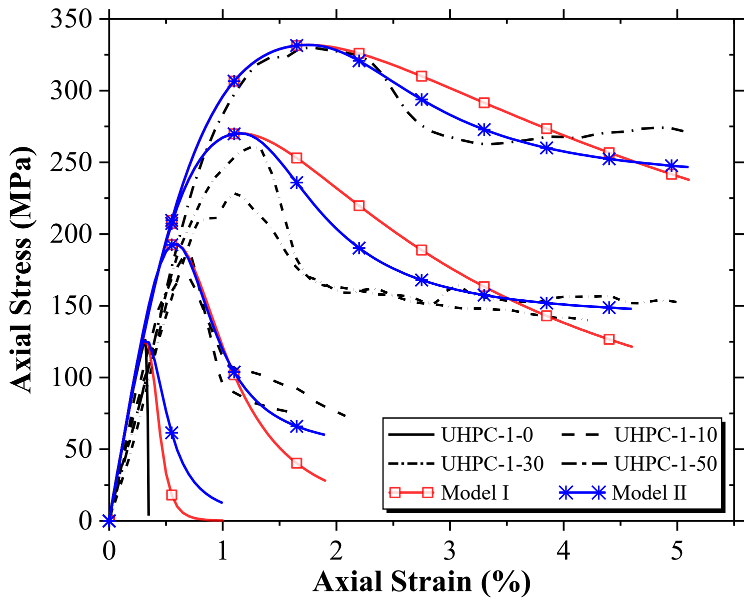

(a) UHPC-1

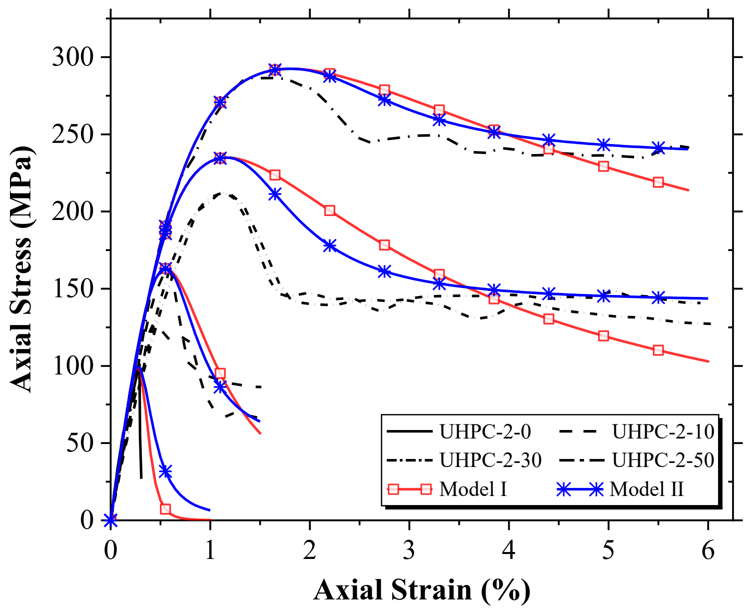

(b) UHPC-2

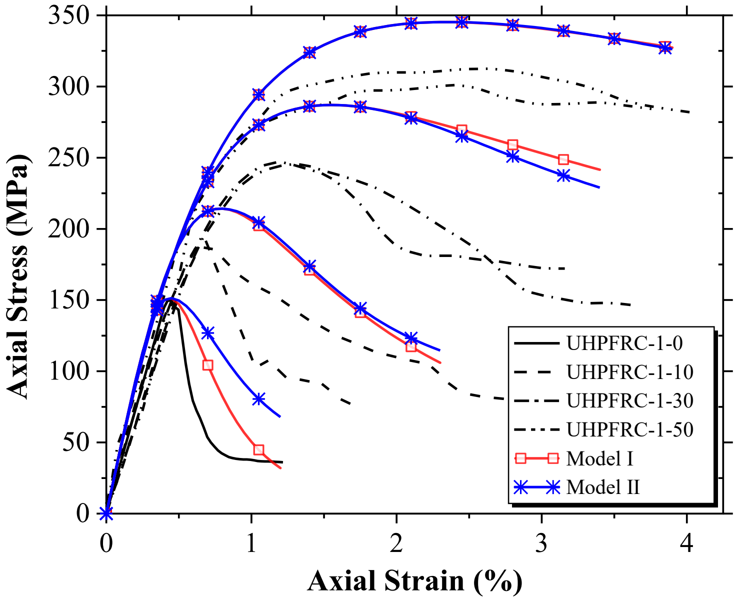

(c) UHPFRC-1

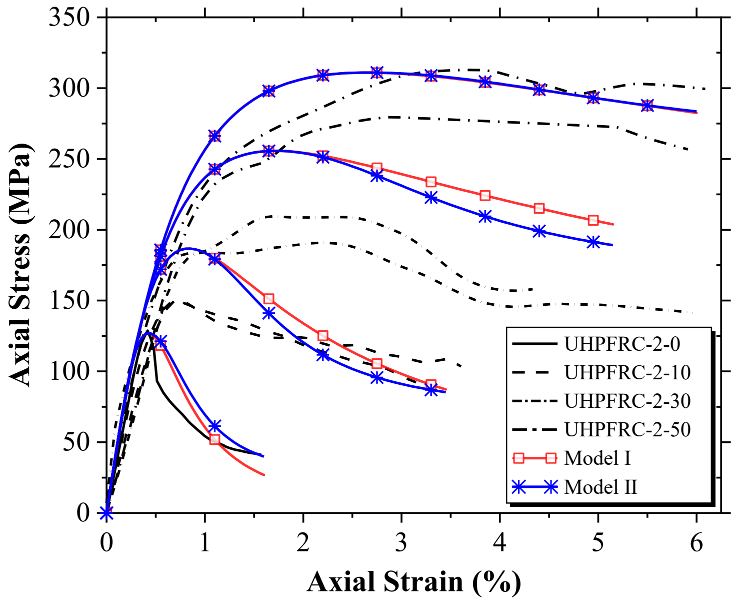

(d) UHPFRC-2

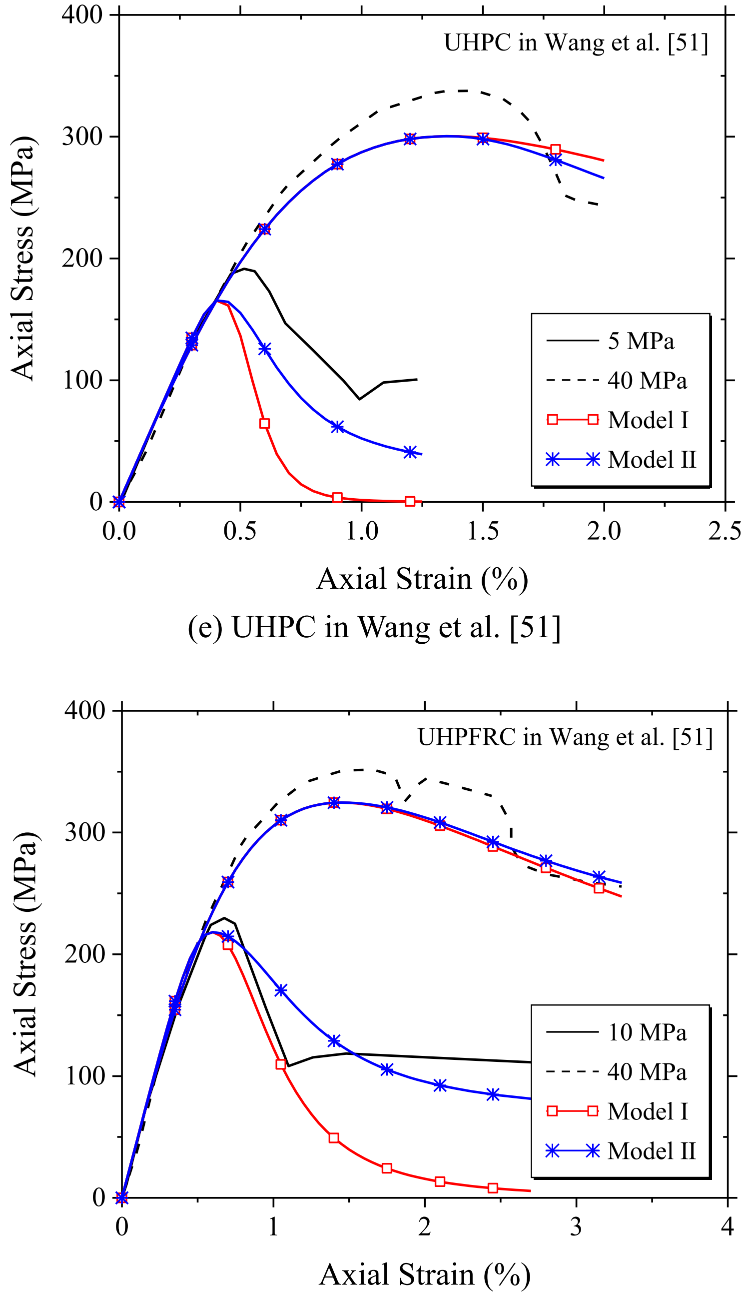

(e) UHPC in Wang et al. [51]

(f) UHPFRC in Wang et al. [51]

Fig. 16. Comparison of axial stress-axial strain curves between test and prediction

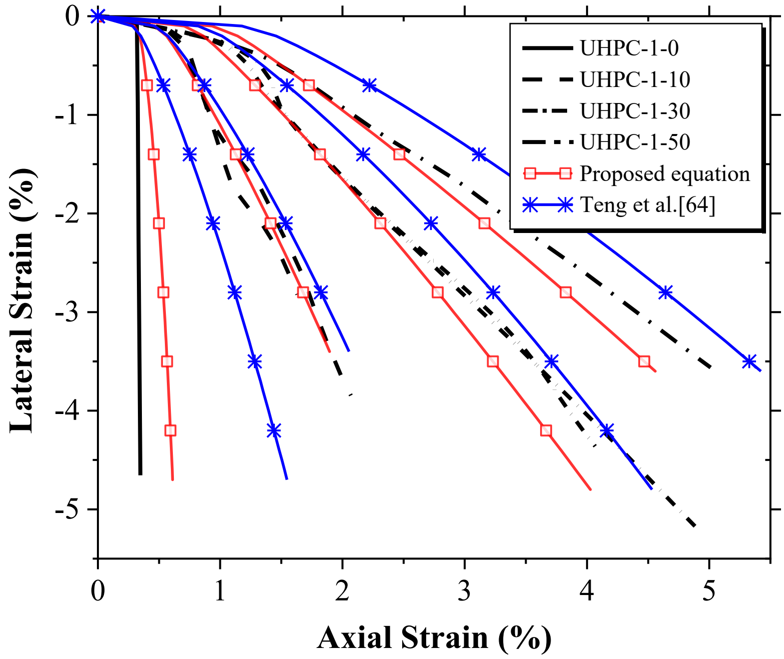

(a) UHPC-1

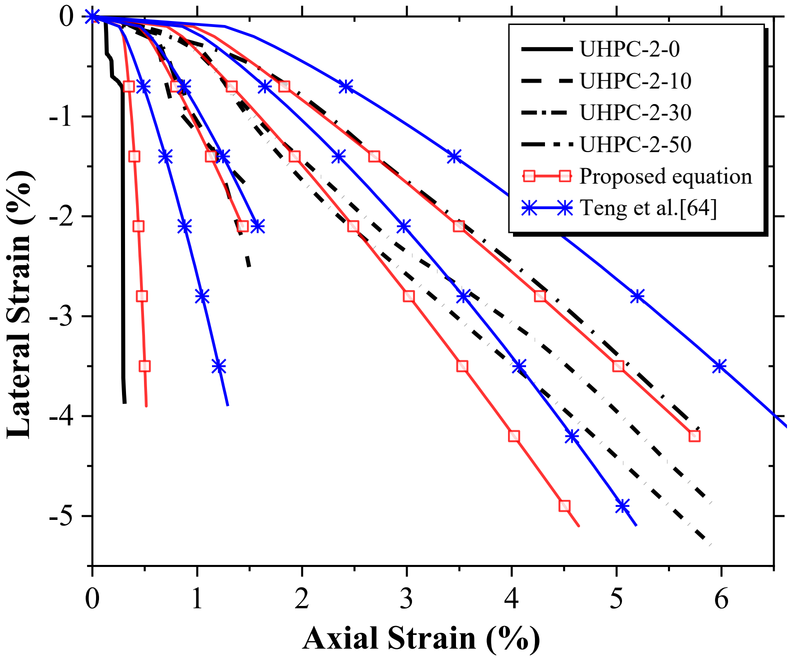

(b) UHPC-2

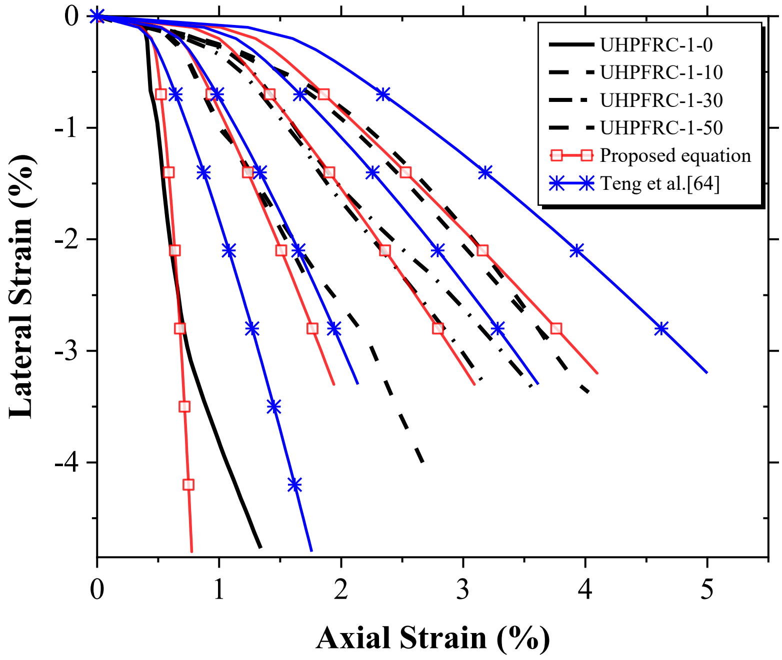

(c) UHPFRC-1

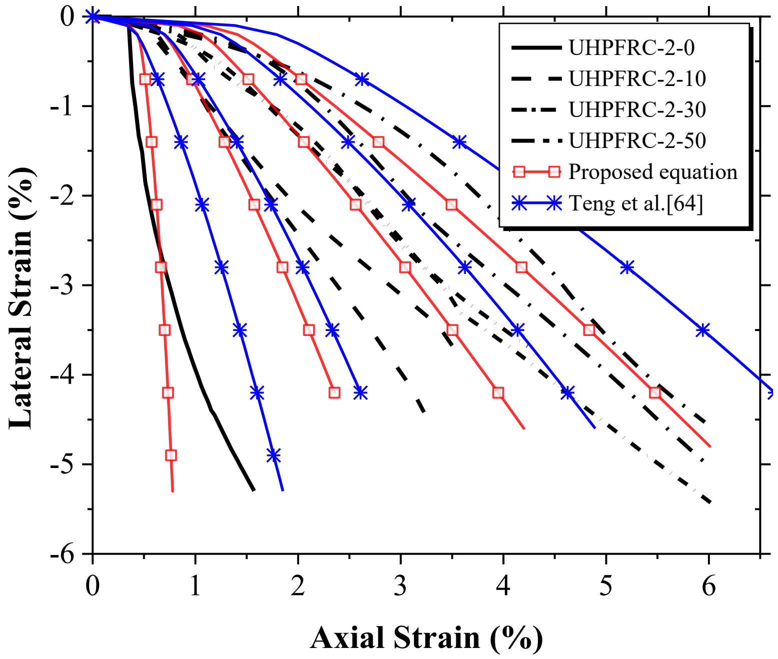

(d) UHPFRC-2

Fig. 17. Comparison of axial strain-lateral strain curves between test and prediction